Jet stream dynamics from a potential vorticity gradient perspective: The method and its application to a kilometre-scale simulation

Author(s):
Bukenberger, Mona; Rüdisühli, Stefan (iD); Schemm, Sebastian (iD)

RESEARCH ARTICLE

Jet stream dynamics from a potential vorticity gradient perspective: The method and its application to a kilometre-scale simulation

Mona Bukenberger | **Stefan Rüdisühli** | **Sebastian Schemm**

Institute for Atmospheric and Climate Science, ETH Zürich, Zurich, Switzerland

Correspondence
Mona Bukenberger, Institute for Atmospheric and Climate Science, ETH Zürich, Universitätstrasse 16, CH-8092 Zürich, Switzerland.
Email: mona.bukenberger@env.ethz.ch

Funding information
H2020 European Research Council, Grant/Award Number: 848698

Abstract

The influence of adiabatic and diabatic processes on the midlatitude circulation is a formidable research question, especially considering their projected changes under global warming. This study presents the prospects, merits, and caveats of a potential vorticity (PV) gradient perspective as a means to disentangle the contributions of adiabatic and diabatic processes affecting the midlatitude circulation. Theoretical considerations reassess the link between the PV gradient and the jet stream. They reveal that the maximum isentropic PV gradient is consistently located on the stratospheric side of the jet, whereas the gradient of ln(PV) is shifted to the tropospheric side but, in general, is better aligned with the jet axis. The stratospheric shift of the PV gradient results from variations in stability across the tropopause, whereas the tropospheric shift of the ln(PV) gradient results from variations in vorticity. Regions of high PV gradient may serve as a proxy for the curvature of the wind field in the case of sufficiently small variations in stability. Otherwise, they depict variations in both wind and thermal stratification along tropopause-intersecting isentropic surfaces. Lagrangian "PV gradient thinking" is demonstrated in two case studies of jet streak evolution in a simulation with 1.1 km grid spacing performed with the graphics-processing-unit-enabled numerical weather prediction model Consortium for Small-Scale Modelling featuring on-line air parcel trajectories. Dry deformation drives the Lagrangian evolution of the PV gradient in the first case, whereas there is a pronounced influence of diabatic modification in the second case. The Lagrangian PV gradient perspective presented offers fresh insight into adiabatic and diabatic processes underlying the midlatitude circulation variability and change.

KEYWORDS
cloud–circulation interactions, jet streak, jet stream, km-scale simulation, midlatitude dynamics, potential vorticity

1 | INTRODUCTION

The jet stream is a circumpolar band of enhanced wind speed in the upper troposphere. Its location, intensity, and meridional meandering influence the evolution of surface weather and are closely interwoven with the occurrence of weather extremes. Locally, the jet stream is "typified by concentrations of stronger wind in the jet streaks, alternating with weaker winds" (Palmén and Newton, 1969, p. 206). The dynamics of the jet have been a long-standing area of research in the field of dynamic meteorology, with its importance as a research topic alternating over the course of the last century between the surface-oriented Bergen School of Meteorology (Bjerknes and Solberg, 1922), the Chicago School (Staff Members of the Univ. of Chicago, 1947), and the Vienna School (Exner, 1925). For a comprehensive review of seminal work, the reader is referred to Palmén and Newton (1969), Shapiro and Keyser (1990), and Davies (1997) and references therein.

In recent years, under the impression of global warming, the scientific community has renewed its attention on the dynamics of the jet stream, focusing in particular on its future location and intensity, as well as on changes in its waviness and its role as a Rossby waveguide (Barnes and Screen, 2015; Francis and Vavrus, 2015; Vallis et al., 2015; Teng and Branstator, 2019; Martin, 2021; Stendel et al., 2021). This entailed a renewed focus on some basic principles of jet dynamics (Wirth, 2020; Wirth and Polster, 2021). One research direction focuses on the interaction between diabatic and adiabatic processes and their importance in shaping the jet stream, as both types of processes are widely considered relevant to its future evolution in a warming climate (Shaw et al., 2016). In particular, increased latent heat release due to increased water vapour capacity in a warmer atmosphere and changes in the meridional temperature gradient in the upper troposphere are expected to alter the jet stream. The former process has the potential, in principle, to cause more explosive extratropical cyclones, which, via associated momentum transport and convergence, may alter the jet stream. On the other hand, changes in the meridional temperature gradient due to amplified polar surface warming are hypothesised to cause a more undulating jet, and eventually more blocked and stationary weather patterns. So far, however, observations and reanalysis data are inconclusive regarding significant trends in the jet position and strength, in particular in the North Atlantic (Barnes and Screen, 2015; Simmons, 2022), but the number of extremely strong jet streaks appears to be increasing (Simmons, 2022).

It follows that a coherent framework capable of separating diabatic from adiabatic processes would be useful for the study of processes underlying trends in the dynamics of the jet. The potential vorticity (PV) perspective provides a suitable, elegant, and powerful foundation. Since the seminal work of Ertel and Rossby (1949) and the invigoration by Hoskins et al. (1985), "PV thinking" has been widely accepted as an insightful framework for the study of adiabatic and diabatic influences on the dynamics of the jet and synoptic-scale weather systems. Its application in the context of upper level wind dates back to at least Kleinschmidt (1955). Owing its success to its conservation under adiabatic flow and its invertibility property, PV has since helped illuminate, among other things, the amplification of extratropical cyclone growth through latent heat release (Gyakum, 1983a; Gyakum, 1983b; Boyle and Bosart, 1986; Stoelinga, 1996; Wernli et al., 2002; Ahmadi-Givi et al., 2004; Binder et al., 2016; Martínez-Alvarado et al., 2016) by generating or sustaining lower tropospheric positive PV anomalies that mutually interact with upper level PV anomalies (Hoskins et al., 1985; Hoskins and Berrisford, 1988; Whitaker et al., 1988; Davis and Emanuel, 1991; Kuo et al., 1991; Reed et al., 1992; Rossa et al., 2000; Čampa and Wernli, 2012; Schemm and Wernli, 2014; Attinger et al., 2021), the evolution and diabatic modification of downstream development via attenuated upper level Rossby wave amplitudes (Grams and Wernli, 2011; Davies and Didone, 2013; Schemm et al., 2013; Oertel et al., 2019b), blocking formation (Pfahl et al., 2015; Steinfeld et al., 2020; Saffin et al., 2021), and surface frontogenesis, including frontal-wave developments (Thorpe and Emanuel, 1985; Joly and Thorpe, 1990; Davies et al., 1991; Bishop and Thorpe, 1994; Appenzeller and Davies, 1996; Fehlmann and Davies, 1999; Dacre and Gray, 2006; Schemm and Sprenger, 2015; Attinger et al., 2021).

A qualitative relationship between the jet and the PV field is often established by considering the interaction between a positive and a negative PV anomaly and the associated horizontal cyclonic and anticyclonic wind fields. A jet streak as a region of enhanced wind speed embedded in the mean westerlies forms in the Northern Hemisphere in the presence of a positive PV anomaly on its poleward side and a negative anomaly on its equatorward side, both of which induce wind fields that locally reinforce the westerlies in between (Bishop and Thorpe, 1994). A blocked flow develops in the reverse case caused by anticyclonic wave breaking, when a streamer of stratospheric high-PV air wraps anticyclonically around low-PV air and eventually forms a PV cut-off (Thorncroft et al., 1993), which leads to a negative PV anomaly on the poleward side and a positive anomaly on the equatorward side of the mean westerlies, which they jointly weaken. The stronger and the closer together two PV anomalies of opposite sign are, the stronger is their combined far-field flow circulation (Bishop and Thorpe, 1994; Thorpe and Bishop, 1995).

This suggests that regions with enhanced PV gradients indicate accelerated horizontal flow. Indeed, Davies and Rossa (1998) established a formal link between the evolution of the jet stream and PV frontogenesis on isentropic surfaces. This has been used to understand jet intensification by considering PV frontogenesis as a consequence of the upper level PV advection (Davies and Rossa, 1998; Archambault *et al.*, 2013; Archambault *et al.*, 2015).

In early studies of isentropic PV development, the upper level flow was often assumed to be quasi-geostrophic and adiabatic; in reality, however, local PV gradients are modified by both adiabatic and diabatic processes. Progress in understanding cross-isentropic vertical mass transport in extratropical cyclones indicates that diabatic processes play a significant role in shaping the upper level PV gradient more often than was assumed previously (Wernli and Davies, 1997; Davies and Didone, 2013; Methven, 2015; Pfahl *et al.*, 2015; Saffin *et al.*, 2021). Recently, Winters (2021) adopted an Eulerian approach by using PV frontogenesis to study the evolution of extreme jets and identified diabatic processes as important contributors to jet streak formation. These findings are a prelude to a Lagrangian study of PV frontogenesis, because the integrated effects of adiabatic and diabatic tendencies along the flow are crucial for understanding the state of the instantaneous PV gradient field along the jet. Eulerian and Lagrangian approaches are not mutually exclusive and generally have different merits and weaknesses. For the PV frontogenesis equation, a Lagrangian approach is a natural choice since it allows for analysing the integrated history of processes acting along the flow, whereas an Eulerian approach only captures the instantaneous effects of deformation on the PV gradient.

Finally, because the PV gradient is known to act as a Rossby waveguide (Martius *et al.*, 2010; Manola *et al.*, 2013; Branstator and Teng, 2017; Wirth, 2020), a PV-gradient-based diagnostic framework also holds appeal for studying drivers of Rossby wave dynamics. A weak jet stream is known to provide little waveguidability, which introduces more uncertainty in the future evolution of large-scale weather systems (Gray *et al.*, 2014; Harvey *et al.*, 2016; Wirth, 2020; Wirth and Polster, 2021). For a strong jet stream, its meridional width determines the wave number and growth rate of the most unstable Rossby waves guided by the jet (Harnik and Chang, 2004). A correct prediction of the strength and position of the jet stream is therefore a prerequisite for accurate daily-to-weekly weather forecasts. The importance of PV gradients in this context has been demonstrated by Gray *et al.* (2014). Idealised studies, such as that by Harvey *et al.* (2016), confirmed that too broad PV fronts (i.e., too small PV gradients) cause reduced Rossby wave phase speeds, and hence errors in numerical weather forecasts.

Based on these considerations, the central ideas of this study are (a) to regard the evolution of the jet stream as adiabatic and diabatic modifications of PV gradients on isentropic surfaces and (b) to investigate the material derivative of isentropic PV gradient tendencies along Lagrangian trajectories of air parcels constituting a jet streak. Combining (a) and (b) allows for disentangling diabatic and adiabatic contributions to jet streak variability by analysing the processes underlying PV gradient dynamics and waveguide formation. We first revisit the theoretical basis of the links between the PV gradient and the jet before establishing an approach to separate adiabatic and diabatic contributions to PV gradient evolution. This approach is then applied to two jet streaks over the North Atlantic in a simulation with 1.1 km grid spacing.

2 | PV GRADIENT FRAMEWORK

We first revisit and extend the theoretical underpinnings of the relationship between the isentropic PV gradient and the flow field, building on Davies (1981) and Davies and Rossa (1998). First, the utility of using the gradients of $\ln(\mathrm{PV})$, $\|\nabla_\theta \ln(\mathrm{PV})\|$, and of PV, $\|\nabla_\theta \mathrm{PV}\|$, as proxies for the flow field is outlined. Second, tendency equations for $\|\nabla_\theta \ln(\mathrm{PV})\|$ and $\|\nabla_\theta \mathrm{PV}\|$ are derived that resemble a frontogenesis equation, and a variant of which is presented that applies to Lagrangian air parcel trajectories and separates adiabatic from diabatic processes acting on $\|\nabla_\theta \mathrm{PV}\|$.

2.1 | PV gradient and jet stream

PV on an isentropic surface is defined as

$$\mathrm{PV} = \frac{\zeta + f}{\sigma}, \tag{1}$$

where ζ is the isentropic relative vorticity, $f = 2\Omega \sin(\phi)$ is the Coriolis parameter, and $\sigma = -(1/g)\partial_\theta p$ is a measure of stratification. Consider a horizontal coordinate system oriented such that the y-axis is parallel to the meridians, where $\nabla_\theta = (\partial_{x_\theta}, \partial_{y_\theta})^\mathrm{T}$ denotes the gradient on an isentropic surface, and assume a zonally uniform horizontal flow $\mathbf{v} \equiv (U, 0)$ and $\|\nabla_\theta \mathrm{PV}\| \equiv |\partial_y \mathrm{PV}|$, where $\|\mathbf{u}\|$ is the standard Euclidean norm of a vector $\mathbf{u}$. Next, the flow is partitioned into a background component (f_0, σ_0, ζ_0) comprised of a constant background flow U_0, vanishing background relative vorticity $(\zeta_0 = -\partial_y U_0 = 0)$, and sufficiently small meridionally varying perturbations $(f', \sigma', \zeta' = -\partial_y U)$ resembling the jet. Here, the horizontal velocity is $U = U_0 + U(y)$, where $U(y)$ describes, similar to in Davies (1981) and Martius *et al.* (2010), the meridional

profile of a zonally uniform jet added on top of a constant background flow.

Consideration is given to the linkage between the PV gradient and the jet stream. In the Northern Hemisphere, where $f_0 > 0$, the second-order Taylor polynomial of the meridional gradient of PV linearised around the previously defined background f_0/σ_0 yields

$$\partial_y \ln(\text{PV}) \approx \frac{1}{f_0} \left[\underbrace{\left(1 - \frac{f' + \zeta'}{f_0}\right) \partial_y(\zeta' + f')}_{A1} \right.$$
$$\left. \underbrace{-\left(1 - \frac{\sigma'}{\sigma_0}\right) \frac{f_0}{\sigma_0} \partial_y \sigma'}_{B1} \right] \qquad (2)$$

for $\partial_y \ln(\text{PV})$ and

$$\partial_y(\text{PV}) \approx \frac{1}{\sigma_0} \left[\underbrace{\left(1 - \frac{\sigma'}{\sigma_0}\right) \partial_y(\zeta' + f')}_{A2} \right.$$
$$\left. \underbrace{-\left(1 - 2\frac{\sigma'}{\sigma_0} + \frac{f' + \zeta'}{f_0}\right) \frac{f_0}{\sigma_0} \partial_y \sigma'}_{B2} \right] \qquad (3)$$

for $\partial_y \text{PV}$. A version of Equation (2) for the Southern Hemisphere, where $f_0 < 0$, is given in Supporting Information Section S1.3. Equations 2 and 3 serve as a starting point for the discussion linking the gradient of PV to the jet stream.

First, the meridional PV gradient is related to the quasi-geostrophic PV gradient. For sufficiently small perturbations – that is, $|\sigma'/\sigma_0| \ll 1$ and $|f' + \zeta'/f_0| \ll 1$ – Equation (2) reduces to

$$\partial_y \ln(\text{PV}) \approx \frac{1}{f_0} \left[\partial_y(f' + \zeta') - \frac{f_0}{\sigma_0} \partial_y \sigma' \right] = \frac{1}{f_0} \partial_y q, \qquad (4)$$

where $q = f - \partial_y U - [(f_0/\sigma_0)\sigma']$ denotes the quasi-geostrophic PV of the system just defined (see Supporting Information Sections S1.1 to S1.3 for a full derivation), with U the quasi-geostrophic wind and $f' = \beta y$. In the Southern Hemisphere, where $f_0 < 0$, the linearisation yields $\partial_y \ln(|\text{PV}|) \approx -\partial_y \frac{1}{f_0} q$. Though the following section focuses on the Northern Hemisphere, all derivations for the Southern Hemisphere are provided in the Supporting Information. From Equation (4) it follows that the formal linkage between the gradient of PV and that of quasi-geostrophic PV requires not only $|\sigma'/\sigma_0| \ll 1$

and $|(f' + \zeta')/f_0| \ll 1$, but also $|2\frac{\sigma'}{\sigma_0} - \frac{f'+\zeta'}{f_0}| \ll 1$, which is not required if the gradient of $\ln(\text{PV})$ is considered.

The next step is to relate the PV gradient to the horizontal wind speed. If meridional variations in stratification are sufficiently smaller than variations in vorticity – that is, $|A1| \gg |B1|$ and $|A2| \gg |B2|$ in Equations 2 and 3 – it follows that

$$\partial_y \ln(\text{PV}) \approx \frac{1 - \frac{f'+\zeta'}{f_0}}{f_0} \partial_y(f' + \zeta'), \qquad (5)$$

$$\partial_y(\text{PV}) \approx \frac{1 - \frac{\sigma'}{\sigma_0}}{\sigma_0} \partial_y(f' + \zeta'). \qquad (6)$$

Finally, in the presence of a sufficiently strong jet stream, the curvature of the flow dominates over β. For example, consider a wind perturbation in the form of a plane wave centred around $y = 0$ with the form $U(y) = U_0 + U' \cos(l_0 y)$ at 45° N. The perturbation amplitude is $U' = 30 \, \text{m·s}^{-1}$ and the jet half-width is 600 km. In this case, $\partial_y^2 U|_{y=0} = -U' l_0^2 \cos(l_0 y)|_{y=0} \approx -1 \times 10^{-9} \, \text{m}^{-1} \cdot \text{s}^{-1}$ and $\beta = 1.6 \times 10^{-11} \, \text{m}^{-1} \cdot \text{s}^{-1}$. Hence, $|\partial_y^2 U(y)| \gg \beta$, so a formal link between $U(y)$ and the PV gradient can be established:

$$\partial_y \ln(\text{PV}) \approx - \frac{1 - \frac{f'+\zeta'}{f_0}}{f_0} \partial_y^2 U, \qquad (7)$$

$$\partial_y(\text{PV}) \approx - \frac{1 - \frac{\sigma'}{\sigma_0}}{\sigma_0} \partial_y^2 U. \qquad (8)$$

Since the stability along an isentropic surface increases from the tropospheric side of the jet to the stratospheric side of the jet, Equation (8) suggests that the maximum PV gradient is shifted towards the stratospheric side of the jet. In contrast, the gradient of $\ln(\text{PV})$ is shifted towards the tropospheric side, but this tropospheric shift is only marginal for sufficiently broad jets since the wind-speed gradient approaches zero close to the jet axis. The amplitude of the stratospheric displacement depends on both the shape of the tropopause and wind-speed variation close to the jet centre. An analytical example can be found in Supporting Information Section S1.5.

Equations 7 and 8 establish a formal link between $\partial_y \ln(\text{PV})$ and $\partial_y \text{PV}$ respectively and the wind speed for small perturbations (i.e., $|\sigma'/\sigma_0| \ll 1$ and $|(f' + \zeta')/f_0| \ll 1$):

$$\partial_y \ln(\text{PV}) \approx - \frac{1}{f_0} \partial_y^2 U, \qquad (9)$$

$$\partial_y \text{PV} \approx - \frac{1}{\sigma_0} \partial_y^2 U. \qquad (10)$$

Because the curvature of the flow field is inherently connected to the dispersion relation of Rossby waves (James, 1995), a potential link between the gradient of ln(PV) and Rossby wave characteristics (such as the waveguidability) emerges. Future studies will need to investigate whether and under what exact assumptions this relationship holds quantitatively or only qualitatively.

Note that in the vicinity of the tropopause, even for $|\sigma'/\sigma_0| \ll 1$, meridional variations in stratification (i.e., $\partial_y \sigma'$) can be large and the terms $B1$ and $B2$ in Equations 2 and 3 cannot be neglected. Therefore, both conditions must be fulfilled and tested independently of each other. For perturbations σ' that are symmetrical with respect to the jet axis, terms $B1$ and $B2$ introduce a stratospheric shift in the gradients of both PV and ln(PV), hence opposing the tropospheric shift in ln(PV) introduced by term $A1$.

From the aforementioned considerations, several insightful conclusions can be drawn for the relationship between a jet stream and the PV gradient. For example, consider a jet profile of the form $U = U_0 + U' \cos(ly)$ with meridional wave number l and meridional wavelength $\lambda = 2\pi/l$. The jet stream is assumed to be the positive part of the perturbation; that is, the region $|ly| \leq \pi/2$. If the linearisation around the background flow should be valid for the entire jet width, it follows using $|(f' + \zeta')/f_0| \ll 1$ that

$$\lambda = \frac{2\pi}{l} \gg \frac{U' 2\pi}{f_0}. \qquad (11)$$

For flow perturbation with amplitude $U' = 10 \, \text{m} \cdot \text{s}^{-1}$ and $f_0 \approx 10^{-4} \, \text{s}^{-1}$ the minimum wavelength is $\lambda \gg 630 \, \text{km}$. Hence, the larger the amplitude of the localised jet is the larger is the minimum wavelength for the linearisation to be valid.

High wind speeds and PV gradients are highly confined laterally. This motivates analysing a smaller region around the jet core for illustrative purposes. For example, for $ly \in [-\pi/5, \pi/5]$, with $U = U_0 + U' \cos(ly)$, the linearisation is valid for all perturbations for which $\lambda \geq (U' 2\pi^2)/5 f_0$, and with $U' = 10 \, \text{m} \cdot \text{s}^{-1}$ it follows that the minimum meridional wavelength λ must exceed 380 km for the linearisation to be valid close to the jet core. The consideration in the previous paragraph is for illustrative purposes and not required for the following applications.

To conclude this first section on the quantitative relationship between the PV gradient and the flow field, we consider again Equations 9 and 10. Under the assumption of a vanishing background flow U_0 and a perturbation in the form of $U' \cos(ly)$, we find

$$\|\nabla_\theta \ln(\text{PV})\| \approx \frac{l^2}{f_0} U' \quad \text{and} \quad \|\nabla_\theta \text{PV}\| \approx \frac{l^2}{\sigma_0} U' \qquad (12)$$

for a single-mode perturbation.

For a wind perturbation modelled by a superposition of a series of modes, $\|\nabla_\theta \ln(\text{PV})\|$ is proportional to the Laplacian of wind speed, but not to the wind speed itself. In such a case, $\|\nabla_\theta \ln(\text{PV})\|$ is dominated by modes with short wavelengths (high wave numbers), which are not necessarily large in amplitude. This is important to keep in mind when interpreting $\|\nabla_\theta \ln(\text{PV})\|$ and renders the spatial filtering an important step in the analysis.

If these conditions are met, regions of high PV gradient serve as a direct proxy for the flow field. Otherwise, they still depict notable variations in both wind and thermal stratification along tropopause-intersecting isentropic surfaces. The adoption of the PV gradient framework itself remains justified in these situations and potentially meaningful for the study of jet dynamics, but a broader definition of the nature of the jet as characterised through a combination of high wind speed and changes in stratification must be invoked. This is particularly likely to occur in regions of enhanced diabatic activity, as shown later in two case studies. Finally, note that though the aforementioned considerations are based on zonal flow, all considerations and approximations are equally valid for a unidirectional flow parallel to PV isolines with $\mathbf{v} \perp \nabla_\theta \text{PV}$ (see also Davies and Rossa, 1998).

2.2 | A Lagrangian perspective on PV frontogenesis

In the previous section we established a rationale for investigating jet dynamics from the perspective of the PV gradient. This section focuses on the tendency equation of the PV gradient, which will later be applied to two illustrative case studies. For an air parcel with a trajectory $\mathbf{x}(t)$ and velocity $(u, v, w)^{\text{T}}$, the material derivative of $\nabla_\theta \text{PV}$ is

$$\underbrace{\frac{D}{Dt}(\nabla_\theta \text{PV})}_{\delta(\nabla_\theta \text{PV})} = \underbrace{\nabla_\theta \left(\frac{D}{Dt} \text{PV} \right)}_{\nabla_\theta(\delta \text{PV}_{\text{DIA}})} - \underbrace{\mathbf{J}_\theta \cdot \nabla_3 \text{PV}}_{\delta(\nabla_\theta \text{PV})_{\theta, \text{DEF}}}, \qquad (13)$$

where D/Dt refers to the material derivative of the full flow field and

$$\mathbf{J}_\theta \cdot \nabla_3 \text{PV} = \begin{pmatrix} \frac{\partial u}{\partial x} & \frac{\partial v}{\partial x} & \frac{\partial w}{\partial x} \\ \frac{\partial u}{\partial y} & \frac{\partial v}{\partial y} & \frac{\partial w}{\partial y} \end{pmatrix}_\theta \cdot \begin{pmatrix} \frac{\partial \text{PV}}{\partial x} \\ \frac{\partial \text{PV}}{\partial y} \\ \frac{\partial \text{PV}}{\partial z} \end{pmatrix} \qquad (14)$$

represents flow deformation and shear. The PV tendency equation takes its conventional form (Pomroy and Thorpe, 2000),

$$\frac{D}{Dt} \text{PV} = \frac{1}{\rho} [(f + \zeta) \cdot \nabla Q + \nabla \wedge \mathbf{F} \cdot \nabla \theta], \qquad (15)$$

where $Q = (D/Dt)\theta$ is the diabatic heating rate, $\mathbf{F}$ represents all non-conservative processes related to diabatic momentum (such as turbulence, friction, and diffusion), and ρ is air density. The first term on the right-hand side (RHS) of Equation (13) contains the tendency of $\nabla_\theta \text{PV}$ caused by diabatic PV modification. Diabatic processes increasing PV on the stratospheric, high-PV side of the jet relative to the tropospheric, low-PV side will increase the PV gradient across the jet, particularly if tropospheric diabatic processes simultaneously decrease PV there, as is the case in the outflow region of the warm conveyor belt (WCB) of a cyclone (Wernli and Davies, 1997; Schemm *et al.*, 2013). We refer to this as *direct-diabatic* $\nabla_\theta \text{PV}$ modification in contrast to the *indirect-diabatic* effect in the second term, which is the $\nabla_\theta \text{PV}$ tendency due to flow deformation and shear that acts also under adiabatic flow conditions. For an equivalent separation of direct- and indirect-diabatic contributions for PV changes, we refer to Davis *et al.* (1993). Wind shear, wind stress, and deformation alter the positions of PV-conserving air parcels with respect to one another, whereby $\nabla_\theta \text{PV}$ increases if parcels are brought closer together and vice versa. In situations of PV non-conservation, the deformation-induced $\nabla_\theta \text{PV}$ tendency contains the additional indirect-diabatic contribution that results from deformation and shear acting on air parcels in which PV is changing. For $\|\nabla_\theta \text{PV}\|$, which is linked to the wind speed, Equation (12), the material derivative is

$$\frac{D}{Dt}\|\nabla_\theta \text{PV}\| = \frac{\langle \nabla_\theta \text{PV}, (\nabla_\theta \frac{D}{Dt}\text{PV} - \mathbf{J_\theta} \cdot \nabla_3 \text{PV})\rangle}{\|\nabla_\theta \text{PV}\|}, \quad (16)$$

where $\langle , \rangle$ denotes the scalar product. Changes in the horizontal wind direction that preserve wind speed will change $\nabla_\theta \text{PV}$ but not $\|\nabla_\theta \text{PV}\|$, which is invariant under rotation of $\nabla_\theta \text{PV}$. Because our primary interest is in wind speed, not wind direction, we focus on $\|\nabla_\theta \text{PV}\|$. In the next section, a practical way to evaluate Equation (16) along parcel trajectories is introduced. For $\|\nabla_\theta \ln(\text{PV})\|$, which is directly proportional to wind speed curvature, Equation (12), and which is large along the jet axis, the material derivative is

$$\frac{D}{Dt}\|\nabla_\theta \ln(\text{PV})\|$$

$$= \frac{\left\langle \nabla_\theta \ln(\text{PV}), \left[\left(\nabla_\theta \frac{D}{Dt}\text{PV} - \mathbf{J_\theta} \cdot \nabla_3 \text{PV}\right) - \frac{D}{Dt}\text{PV} \cdot \nabla_\theta \ln(\text{PV})\right]\right\rangle}{\|\nabla_\theta \text{PV}\|} \quad (17)$$

$$= \frac{1}{\text{PV}}\left(\frac{D}{Dt}\|\nabla_\theta \text{PV}\| - \frac{D}{Dt}\text{PV}\|\nabla_\theta \ln(\text{PV})\|\right). \quad (18)$$

2.3 | Adiabatic and diabatic Lagrangian PV gradient changes

In this section, we outline a Lagrangian-based method to decompose changes in $\|\nabla_\theta \text{PV}\|$ into adiabatic and diabatic contributions that is straightforward, complete, and applicable to model output data. As long as PV is positive, the decomposition presented is equally valid for changes in $\|\nabla_\theta \ln(\text{PV})\|$. Though the trajectories are computed on-line as part of the model simulation, the PV gradient is computed offline because a direct computation of the RHS of Equations (16) and (17) during a model simulation would introduce substantial computational overhead. One reason is that adherence to theory requires low-pass filtering of PV and derived fields on isentropic surfaces, which necessitates global communication across the computational subdomains, before tracing the filtered variables along on-line air parcel trajectories. We avoid this by performing the decomposition offline based on PV from regular model output data, which also obviates the need for additional, computationally expensive variables traced along the on-line trajectories. Another aspect that calls for caution is that the second term on the RHS of the PV frontogenesis equation includes contributions from deformation and shear acting on diabatically modified PV, which is an indirect diabatic contribution to PV frontogenesis. To overcome this, we define adiabatic, direct-diabatic and indirect-diabatic PV frontogenesis contributions. In the following, PV always refers to low-pass filtered PV to ensure adherence to the scale separation introduced in Section 2.1.

2.3.1 | Net PV gradient change

We consider the positions of an air parcel trajectory $\mathbf{x}(t_i)$ at two times t_0 and $t_1 = t_0 + \delta t$. For the remainder of this section, we are interested in PV gradient tendencies at the end location of a forward trajectory; that is, position $\mathbf{x}(t_1)$ at time t_1. The net change of $\|\nabla_\theta \text{PV}\|$ along a trajectory is defined as the difference between the values at the start and end points:

$$\delta\|\nabla_\theta \text{PV}\|[\mathbf{x}(t_1)] \equiv \|\nabla_\theta \text{PV}\|[\mathbf{x}(t_1)]$$

$$- \|\nabla_\theta \text{PV}\|_{\text{ADV}}[\mathbf{x}(t_1)], \quad (19)$$

where the second term on the RHS is the advective PV gradient, which is computed by projecting the $\|\nabla_\theta \text{PV}\|$ values from $\mathbf{x}(t_0)$ to $\mathbf{x}(t_1)$ and corresponds to PV-gradient-conserving advection from t_0 to t_1; that is, $\|\nabla_\theta \text{PV}\|_{\text{ADV}}[\mathbf{x}(t_1)] \equiv \|\nabla_\theta \text{PV}\|[\mathbf{x}(t_0)]$.

2.3.2 | Adiabatic PV gradient change

If PV is conserved, changes in the PV gradient result solely from flow deformation and shear. Assuming PV conservation along the flow, the adiabatic contribution to the PV gradient change is the difference between the gradient within the flow at two times t_0 and t_1. The PV gradient is recomputed at $\mathbf{x}(t_0)$ and $\mathbf{x}(t_1)$ based on the initial PV value from $\mathbf{x}(t_0)$, which isolates the changes that result exclusively from deformation or shear. More formally, the adiabatic component is the difference between the gradient of advected PV and the advected PV gradient:

$$\delta\|\nabla_\theta PV\|_{\text{ADI}}[\mathbf{x}(t_1)] = \|\nabla_\theta PV_{\text{ADV}}\|[\mathbf{x}(t_1)]$$
$$- \|\nabla_\theta PV\|_{\text{ADV}}[\mathbf{x}(t_1)]. \quad (20)$$

The idea of an advected PV is inspired by its use in earlier studies in which PV changes along trajectories were decomposed into contributions from different diabatic processes (Wirth and Egger, 1999; Gray, 2006; Chagnon *et al.*, 2013; Chagnon and Gray, 2015; Crezee *et al.*, 2017; Attinger *et al.*, 2019; Spreitzer *et al.*, 2019a). The recalculation of the gradient based on advective PV requires a dense trajectory field, which is possible due to the large number of on-line trajectories used in this study.

2.3.3 | Diabatic PV gradient change

The total diabatic contribution corresponds to the difference between the PV gradient and the gradient of advected PV:

$$\delta\|\nabla_\theta PV\|_{\text{DIA}}[\mathbf{x}(t_1)] = \|\nabla_\theta PV\|[\mathbf{x}(t_1)]$$
$$- \|\nabla_\theta PV_{\text{ADV}}\|[\mathbf{x}(t_1)]. \quad (21)$$

In the case of PV conservation the term would be zero. The diabatic PV gradient change has two components, because diabatic changes may result solely from PV non-conservation with no simultaneous change in the relative positions of air parcels with respect to each other (deformation- and shear-free flow), or from deformation and shear acting on PV that is simultaneously not conserved. We refer to the first case as the direct-diabatic and to the second as the indirect-diabatic PV gradient change.

In a deformation- and shear-free flow, changes in $\|\nabla_\theta PV\|$ will result exclusively from direct-diabatic $\nabla_\theta PV$ modification. Thus, we calculate the direct-diabatic change of $\|\nabla_\theta PV\|$ by assuming zero deformation and shear, in the spirit of the adiabatic contribution, which is computed assuming PV conservation. To do so, we assume that, in the absence of deformation and shear, the relative

positions of air parcels with respect to each other are constant over time; that is, the same as at the start locations. Hence, the PV gradient is recomputed at the start location but using the PV value from the end location. In practice, PV values from time t_1 are advected backward along the forward trajectories from their end positions $\mathbf{x}(t_1)$ back to their start positions $\mathbf{x}(t_0)$. After interpolating this backward-advected $PV_{\text{ADV,BW}}$ onto isentropic surfaces, we recompute the PV gradient and then interpolate it back to the start positions $\mathbf{x}(t_0)$ and advect it forward to $\mathbf{x}(t_1)$. Subtracting the regular advected PV gradient yields the direct-diabatic contribution:

$$\delta\|\nabla_\theta PV\|_{\text{DIA,DIR}}[\mathbf{x}(t_1)] = \|\nabla_\theta PV_{\text{ADV,BW}}\|_{\text{ADV}}[\mathbf{x}(t_1)]$$
$$- \|\nabla_\theta PV\|_{\text{ADV}}[\mathbf{x}(t_1)]. \quad (22)$$

Finally, changes in the relative positions of air parcels with respect to each other with simultaneously changing PV correspond to the indirect-diabatic effect, which is defined as the difference between the direct-diabatic, Equation (21), and the net diabatic, Equation (22), changes:

$$\delta\|\nabla_\theta PV\|_{\text{DIA,IND}}[\mathbf{x}(t_1)] = \delta\|\nabla_\theta PV\|_{\text{DIA}}[\mathbf{x}(t_1)]$$
$$- \delta\|\nabla_\theta PV\|_{\text{DIA,DIR}}[\mathbf{x}(t_1)]. \quad (23)$$

Intuitively, the direct-diabatic effect is expected to be large in regions characterised by low shear and deformation but with simultaneous PV non-conservation, which is the case in the jet stream core. The indirect-diabatic effect is expected to be large in regions of high wind shear and deformation with simultaneous PV non-conservation, which is the case at the jet stream edges, especially on the tropospheric side over an active cold front.

2.3.4 | Closing remarks

The direct- and indirect-diabatic contributions by definition add up to the total diabatic change $\delta\|\nabla_\theta PV\|_{\text{DIA}}$. To prove, in turn, that the diabatic and adiabatic contributions account for total $\delta\|\nabla_\theta PV\|$, we combine Equations 20 and 21, which yields

$$\delta\|\nabla_\theta PV\|_{\text{DIA}}[\mathbf{x}(t_1)] + \delta\|\nabla_\theta PV\|_{\text{ADI}}[\mathbf{x}(t_1)]$$
$$= \|\nabla_\theta PV\|[\mathbf{x}(t_1)] - \|\nabla_\theta PV\|_{\text{ADV}}[\mathbf{x}(t_1)]$$
$$= \delta\|\nabla_\theta PV\|[\mathbf{x}(t_1)]. \quad (24)$$

Though the budget is formally closed, numerical uncertainties affecting all terms emerge in any implementation. They affect the positioning of the trajectories as well as

the PV and PV gradient fields due to spatial interpolation, low-pass filtering, and gradient calculation. The low-pass filter and the calculation of $\|\nabla_\theta PV\|$ require dense enough parcel trajectories coverage at both t_0 and t_1. Though the separation into adiabatic and diabatic contributions is possible based on either forward or backward trajectories, the distinction between direct- and indirect-diabatic contributions is not easily achieved with backward trajectories started from the jet streak region. The reason is that computing the low-pass filter and gradients on an isentropic surface of a field interpolated from trajectories requires dense enough trajectories coverage around this surface. In our experience, this is not given when computing the gradient of backward-advected PV at t_0 based solely on trajectories that constitute a jet streak at t_1. By contrast, a massive number of forward trajectories started at t_0, only some of which will end in the jet streak, provide dense enough coverage to compute $\|\nabla_\theta PV_{ADV,BW}\|$ on sufficient isentropic surfaces to envelop the start and end points of the trajectories. In our 1.1 km simulation covering a large part of the North Atlantic sector, trajectories were started repeatedly throughout the domain from 352,692 start points (see Table 3).

3 | DATA AND METHODS

3.1 | Model and simulation

The simulation has been conducted with the graphics processing unit (GPU)-enabled Consortium for Small-Scale Modelling (Consortium for Small-Scale Modelling; COSMO, 2022) weather and climate prediction model (Doms and Schättler, 1999; Steppeler *et al.*, 2003; Fuhrer *et al.*, 2014; Lapillonne and Fuhrer, 2014) version 6.0 running in single precision on GPU accelerators, with adaptations to the model code as described in the following. The model domain covers the eastern North Atlantic (Figure 1) with a resolution of 0.01° (~1.1 km), which allows for explicit convection. The simulation set-up is summarised in Table 1. Initial and boundary conditions are operational European Centre for Medium-Range Weather Forecasting (ECMWF) Integrated Forecasting System high-resolution analysis fields with 6 hr temporal and 0.1° (~11 km) spatial resolution (ECMWF, 2022a; ECMWF, 2022b; ECMWF, 2022c). For performance reasons, the simulation is composed of three separate meteorologically identical runs: one with regular model output but no trajectories, and two with trajectories over different height ranges. They were carried out at the Swiss National Supercomputing Centre (CSCS) in Lugano, Switzerland, on Piz Daint, a Cray XC50 system with NVIDIA Tesla P100 GPUs (CSCS, 2022).
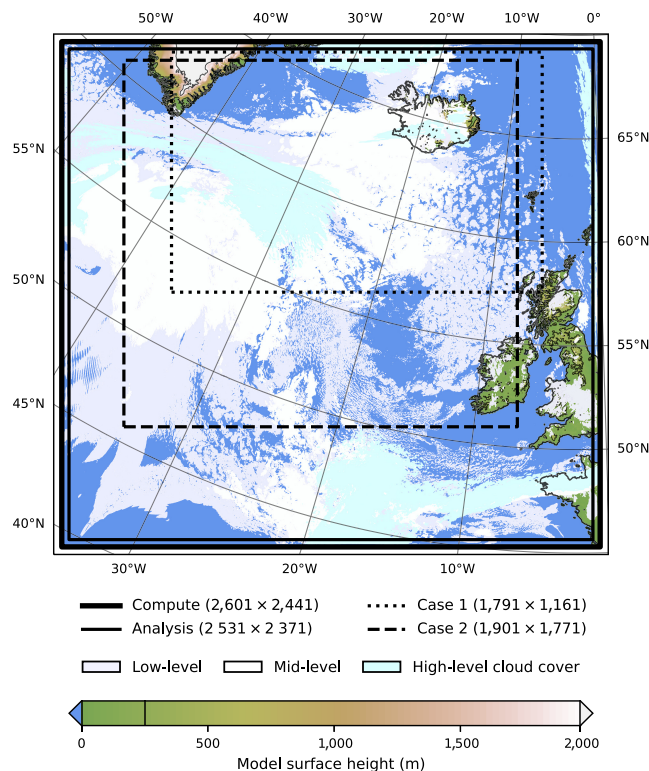

FIGURE 1 Model domain, topography, and sample cloud cover of the simulation with a horizontal resolution of 0.01° (~1.1 km). Solid frames show the extents of the computational domain in bold along with the analysis domain. Dashed and dotted frames indicate the subdomains used in the plots accompanying the two case studies. The line legend labels contain the horizontal grid size of the respective domain ($n_{lon} \times n_{lat}$). Low-, mid-, and high-level cloud cover at 0600 UTC on September 22, 2016, as obtained from the model output are shown in white and light bluish colours, overlaying the ocean in blue and the model topography in green to brownish colours. [Colour figure can be viewed at wileyonlinelibrary.com]

Selected metrics on the simulation runs are listed in Table 2.

On-line trajectories with a duration of 12 hr were started every 3 hr from 352,692 start points during most of the simulation. Details on the trajectories set-up are shown in Table 3, and the numbers of trajectories used in the analysis in Table 4. Though the trajectory positions were updated every 7.5 s with the same frequency as the model, variable tracing (i.e., interpolation of model fields to the trajectories) and output was only done every 60 s for performance reasons. Six standard fields were traced along the trajectories (u, v, w, p, T, q_v), whereas PV and related fields were interpolated offline from model output fields available every hour (e.g., see Figure 9).

Dissipation of an initial shock upon model initialisation required a spin-up period of 1–2 days, well short of the 51 hr when the first trajectories analysed in this study were started at 0300 UTC on September 22, 2016, which is about

TABLE 1   Summary of the set-up of the Consortium for Small-Scale Modelling simulation.

Grid size	$2{,}601 \times 2{,}441 \times 80$
Grid points	507,923,280
Horizontal resolution	0.01° (~1.1 km)
Time step	7.5 s
Convection	Fully explicit
Microphysics	Prognostic cloud water, cloud ice, rain, snow, and graupel (Reinhardt and Seifert, 2006)
Initialisation	September 20, 2016, 0000 UTC
Integration time	96 hr

TABLE 2   Selected metrics on the output, trajectories, and footprint of the three meteorologically identical Consortium for Small-Scale Modelling simulation runs[a] performed for this study.

	MOD	TR1	TR2
Written two-dimensional slices[b]	73,710	192	192
Total trajectories	0	4,702,560	2,351,280
Run time (h:mm:ss)	4:36:04	7:36:03	5:03:58
GPU nodes	110	150	120
Node hours	506.1	1,140.1	607.9
Mean GPU usage[c] (%)	52.00	41.73	45.25
Mean memory usage[c,d] (MiB)	14,995	13,511	13,472
Total memory usage[c,d] (GiB)	1,610.791	1,979.150	1,578.750
Energy consumption (kJ)	310,168	548,353	324,864

Abbreviations: GPU, graphics processing unit; MOD, model output; TR1, first run with trajectories; TR2, second run with trajectories.

[a]The simulations were performed on a Cray XC50 system with NVIDIA Tesla P100 GPUs.

[b]Refers to the number of times a horizontal slice has been written to disk (e.g., writing two 80-level three-dimensional fields three times corresponds to 480 two-dimensional slices).

[c]Mean GPU and memory usage are per node, each of which has 16 GB of memory.

[d]1 MiB corresponds to $(2^{10})^2$ bytes, and 1 GiB corresponds to $(2^{10})^3$ bytes.

when cyclone *Vladiana* enters the domain (see Section 4). Qualitative comparisons of our simulation with synoptic fields and other simulations of the same time period (Oertel *et al.*, 2019a) reveal a positive surface-pressure bias, but an overall accurate representation of the cyclone and the jet stream.

In order to compute on-line trajectories as part of our GPU-accelerated simulation, we ported the existing

TABLE 3   Summary of the trajectories set-up.

Trajectory duration	12 hr
Start interval	3 hr
First start	24 hr
Last start	84 hr
Start grid spacing	$27.5 \times 27.5 \times 0.5 \text{ km}^3$
Start points	352,692
Total trajectories	7,053,840
Total trajectory times	84,646,080 hr
Advection time step	7.5 s
Tracing time step	60 s
Traced fields	u, v, w, p, T, q_v

TABLE 4   Number of trajectories used at various stages of the analysis for both cases.[a]

	Case 1		Case 2		
	320 K	Jet A1	320 K	Jet A2	Jet B
Selected at t_1	28,830	692	31,596	1,232	764
Selected at t_0	248,445	66,028	234,823	159,551	
Started at t_0	352,692		352,692		

[a]The first row contains the number of trajectories that at time t_1 end within ± 3 K of the 320 K isentropic surface. The second row contains the number of trajectories required at time t_0 to envelop the start positions of the first-row trajectories densely enough to interpolate values from them onto isentropic surfaces and from there onto the start positions of the first-row trajectories (see Section 3.2.2 for details). The third row contains the total number of trajectories that were started at t_0 of the respective case, which are supersets of those in the respective columns of the first two rows.

on-line air parcel trajectory module (Miltenberger *et al.*, 2013) to GPUs using OpenACC directives, similar to what Lapillonne and Fuhrer *et al.* (2014) did for selected physical parametrisations. Efficient execution on GPUs required code refactoring, like breaking up a loop over all trajectories that spanned the entire module into successive smaller loops performing specific tasks, like advection, tracing, and output. Our code is available to licensed COSMO users upon request.

3.2 | Data analysis

3.2.1 | Low-pass filtering

The model with a horizontal grid resolution of 1.1 km is able to resolve mesoscale flow features such as
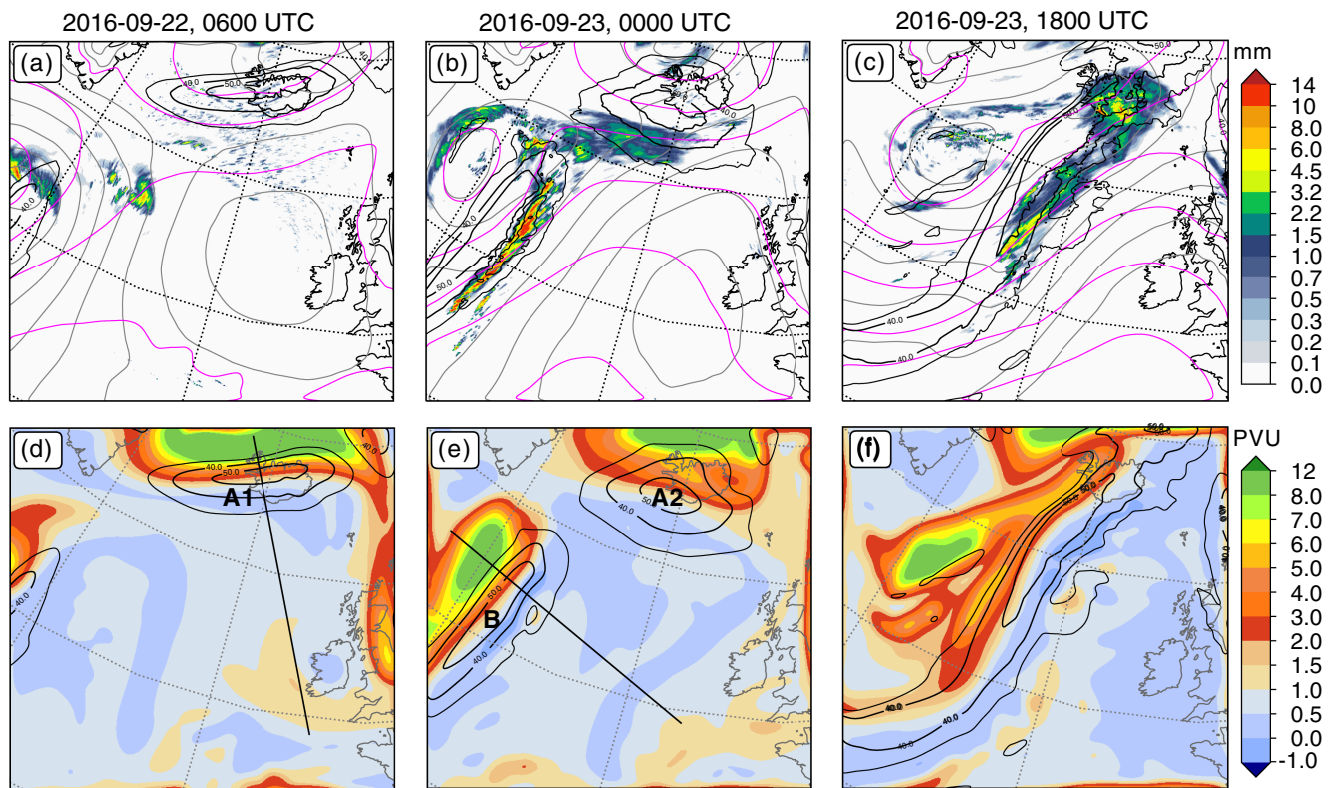
FIGURE 2 Synoptic situation in the simulation at (a, d) 0600 UTC on September 22, (b, e) 0000 UTC on September 23, and (c, f) 1800 UTC on September 23, 2016. (a–c) Hourly precipitation in colours; mean-sea-level pressure as grey contours from 1,000 to 1,050 hPa every 10 hPa; horizontal wind speed at 320 K as black contours for 30, 40, and 50 m·s^{-1}; and 500 hPa geopotential height as purple contours from 5,600 to 6,300 m every 100 m. (d–f) The 200 km low-pass filtered potential vorticity (PV) at 320 K in colours; and 200 km low-pass filtered horizontal wind speed at 320 K as black contours for 30, 40, and 50 m·s^{-1}. Note that only a part of the whole domain is shown (see Figure 1). PVU: PV units. [Colour figure can be viewed at wileyonlinelibrary.com]

convection-induced PV dipoles, which cause locally high values of $\|\nabla_\theta \mathrm{PV}\|$. Meanwhile, the link between $\|\nabla_\theta \mathrm{PV}\|$ or $\|\nabla_\theta \ln(\mathrm{PV})\|$ and horizontal wind speed is valid for quasi-geostrophic flow. In Section 2, we discussed for which plain-wave perturbations linearising $\ln(\mathrm{PV}_\theta)$ is justified in order to link it to quasi-geostrophic PV. This revealed that application of the PV gradient framework requires eliminating small-scale features. After testing several filter wavelengths (not shown), we chose a Gaussian low-pass Fourier filter with a cut-off wavelength of 200 km for this study. Though this eliminates individual mesoscale vortices induced by convective clouds, their collective effects at larger scales are retained as structures such as elongated PV dipoles that may affect the jet streak dynamics. To apply the framework at even larger scales (e.g., in global datasets), longer cut-off wavelengths of up to around 500 km may be more appropriate. For the Eulerian analysis in Section 4.1, PV and velocity fields on isentropic surfaces (Figure 2) are obtained by interpolating the respective variable from model levels onto

an isentrope, then removing grid points in the 0.35°-wide nudging zone and finally applying the low-pass filter.

3.2.2 | Lagrangian-based fields

Fields obtained by interpolating values from trajectories to a regular grid are referred to as Lagrangian-based fields (see Section 2.3 for details). In order to quantify the creation and destruction of PV or PV gradients along the flow between two times, we subtract passively advected values from the Eulerian field at target time. Advected fields like $\mathrm{PV_{ADV}}$ are obtained by interpolating the Eulerian field to the start positions of the trajectories, projecting them to the end positions, and then interpolating back onto a regular grid. Similarly, computing the backward-advected field $\mathrm{PV_{ADV,BW}}$ involves interpolating the Eulerian values to the end positions of the trajectories, projecting these values to the start positions, and then interpolating back onto a regular grid. To illustrate this,

we present the specific steps required to compute the isentropic gradient of advected PV, $\nabla_\theta PV_{ADV}$, at time t_1 on the 320 K isentropic surface:

1. At time t_1, select all trajectories that end in close vicinity to the isentropic surface of interest; that is, in the layer 320 ± 3 K.
2. At time t_0, select as many isentropic surfaces (with a spacing of 5 K) as necessary to envelop the start positions of these trajectories.
3. Linearly interpolate the Eulerian PV field at t_0 to these isentropic surfaces and apply the 200 km low-pass filter, then linearly interpolate this filtered PV_θ field to the start positions of the trajectories selected in step 1.
4. Advect conserved PV along the trajectories from time t_0 to t_1 by projecting the values from the start positions $\mathbf{x}(t_0)$ of the trajectories to their end positions $\mathbf{x}(t_1)$ 3 h later.
5. Perform multi-linear interpolation of these PV_{ADV} values to the 320 K surface, apply the 200 km low-pass filter, and compute the horizontal gradient to obtain $\nabla_\theta PV_{ADV}$.

Other Lagrangian-based fields are computed analogously by combining the necessary basic steps in the appropriate order. When comparing Lagrangian-based fields like PV_{ADV} with Eulerian model fields, we have to process the latter analogously to account for sampling effects in the former. To this end, they are first interpolated to the trajectory positions at the respective time step, then from there to the isentropic surface of interest. This puts them on an equal footing by eliminating information that is not present in the Lagrangian-based fields simply due to the spatial distribution of the trajectories. To verify the large-scale accuracy of these "pseudo-Lagrangian-based" fields, compare Figures 3 and 8a with the original Eulerian fields in Figure 2.

4 | CASE STUDIES

The utility of the Lagrangian PV gradient framework is demonstrated by analysing two jet streaks over the eastern North Atlantic on September 22–23, 2016, when extratropical cyclone *Vladiana* occurred during the North Atlantic Waveguide and Downstream Impact Experiment campaign (Schäfler *et al.*, 2018). Previous studies have investigated the temporal evolution and structural details of the storm (e.g., Oertel *et al.*, 2019a; Oertel *et al.*, 2019b). In this study, we analyse a COSMO simulation with 1.1 km resolution to address the following questions:

• How do PV gradients evolve in the vicinity of jet streaks?

• What role do adiabatic and diabatic processes play in this?

4.1 | Synoptic overview

The synoptic situation is shown in Figure 2. On September 22, a jet streak is located over Iceland ("A1" in Figure 2d), associated with an upper level trough north of a surface high-pressure system that is located west of the British Isles (Figure 2a). The near absence of precipitation, in particular below the Iceland jet streak, indicates that moist diabatic processes are unlikely to play a large role in the evolution of the jet streak. Half a day later, as cyclone *Vladiana* has entered the domain (Figure 2b), a second jet streak emerges aligned with the surface cold front ("B" in Figure 2e). WCB air masses ascending from the warm sector of the intensifying cyclone feed an increasingly intense ridge downstream (Figure 2f). As the cyclone propagates northeastwards, precipitation intensifies close to the surface fronts (Figure 2b,c), indicating an increasing relevance of diabatic processes for cyclone development. The Iceland jet streak, while staying in place, has broadened considerably and rotated anticyclonically into a zonal orientation ("A2" in Figure 2e). The *Vladiana* jet streak ("B" in Figure 2e) intensifies along with the cyclone as the latter moves towards Iceland between 0000 UTC and 1200 UTC on September 23. During the following hours, the two jet streaks start to interact (Figure 2c) and finally merge into a coherent meridionally elongated jet band (Figure 2f). During the merger, intense surface precipitation (Figure 2b,c) indicates substantial diabatic PV modification with the potential to alter the PV gradient. In the following sections, the two jet streaks will be studied from a Lagrangian PV gradient perspective.

4.2 | Case 1: Iceland jet streak

Before starting the first Lagrangian PV gradient analysis based on the on-line trajectories described in Section 3, two points call for attention. First, the choice of 3 hr for the analysis time window constitutes a trade-off between a sufficiently large duration to capture the main processes on the one hand and the number of complete trajectories of that length on the other hand. Given the size of our model domain, air parcel trajectories that end in a jet streak (defined by wind speed above 40 m·s^{-1} at 320 K; see Section 3), have typically spent several hours, but seldom more than 6 hr in the computational domain. Most of the changes in PV and derived fields occur during the last 2–3 hr before the trajectories enter a jet streak (not shown). We chose 3 hr as the analysis time window,
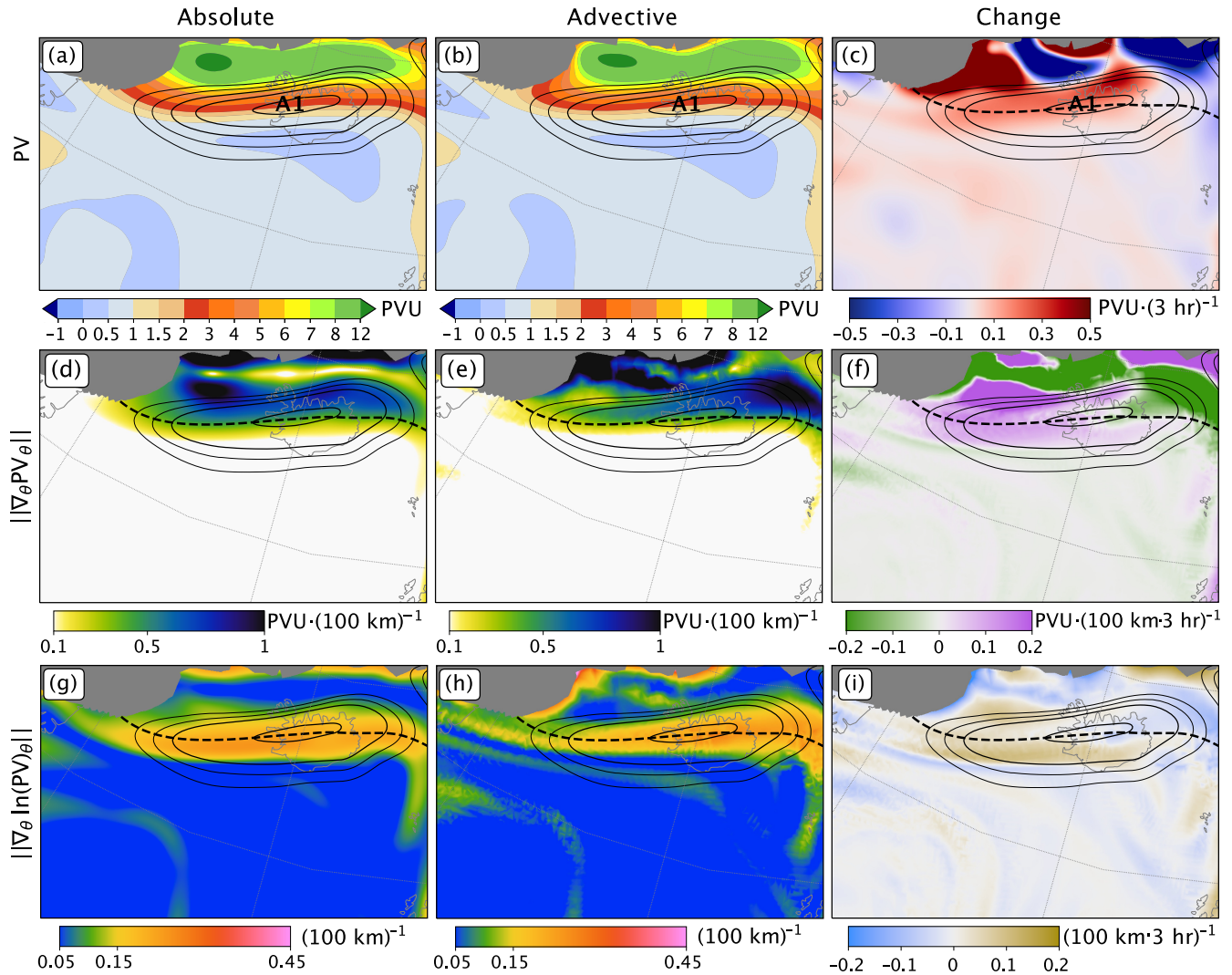
FIGURE 3   Lagrangian-based fields at 0600 UTC on September 22, 2016, at 320 K. Shown in colours are (a) absolute potential vorticity (PV), (b) 3 hr advected PV, and (c) difference between the two; (d) absolute $\|\nabla_\theta PV\|$, (e) 3 hr advected $\|\nabla_\theta PV\|$, and (f) difference between the two; (g) absolute $\|\nabla \ln(PV)\|$, (h) 3 hr advected $\|\nabla \ln(PV)\|$, and (i) difference between the two. Horizontal wind speed is shown as black solid contours for 30 m·s^{-1}, 35 m·s^{-1}, 40 m·s^{-1}, and 50 m·s^{-1}, along with (c–i) the 2PVU dynamical tropopause at 320 K as a black dashed contour. Grey areas indicate regions where there are no trajectories or, for (g–i), where ln(PV) is not well defined (PV $\leq$ 0 PVU). PVU: PV units. [Colour figure can be viewed at wileyonlinelibrary.com]

and thus trajectory duration, which constitutes a good compromise.

Second, note that all fields in Figure 3 are Lagrangian based (see Section 3 for details); even the instantaneous fields are first interpolated to the positions of the air parcel trajectories and from there onto an isentropic surface, for consistency with truly Lagrangian-based fields, as described in Section 3.2.2.

We analyse the Iceland jet streak at 0600 UTC on September 22, 2016, based on trajectories started at 0300 UTC on the same day. We first compare absolute PV and advective PV (Figure 3a,b). The former represents the instantaneous PV field and the latter the PV field advected along the 3 h trajectories under the assumption

of PV conservation (see Section 3.2.2 for details). The two fields are almost identical, with PV changes of δPV < 0.1 PVU in most of the target region (Figure 3c).[1] The tropospheric side of the jet streak exhibits very small positive PV changes that increase towards the stratospheric side to δPV $\geq$ 0.3 PVU ·(3 hr)$^{-1}$.

The jet axis is aligned with an elongated band of high $\|\nabla_\theta PV\|$, which is displaced by around 50–100 km towards the stratospheric side of the jet (Figure 3d). Overall, and

---

[1]High values outside the jet streak boundary close to the northern model domain boundary are an exception. However, since these are close to the boundary zone where the fields are nudged towards the driving fields, they are not further considered in this analysis.

especially in jet entrance and exit regions, the absolute and advected $\|\nabla_\theta PV\|$ fields differ, which indicates that the PV gradient along the air parcel trajectories was not preserved during the preceding 3 hr. The air parcels in the jet entrance experienced an increase in $\|\nabla_\theta PV\|$, those in the exit region a decrease, and those in-between no substantial change (Figure 3f). This reflects the acceleration and deceleration of the air parcels as they traverse the jet streak. At the entrance, air parcels arrive from regions with lower PV gradients and lower wind speeds (red dots in Figure 4a), leading to an increase in the PV gradient along the flow. Given the flow is confluent at the jet entrance and diffluent at the exit, causing air parcels with different PV to move closer together and further apart, an increase and decrease in the PV gradient is expected respectively in the absence of any diabatic processes (Figure 4a,b). The mean wind speed along all air parcel trajectories ending in the jet entrance region (solid black line in Figure 4c) increased in proportion to the mean PV gradient (solid red dots), whereas both the wind speed and $\|\nabla_\theta PV\|$ decreased along those trajectories ending in the jet exit region. We conclude that, for the Iceland jet streak, the ageostrophic component of the horizontal wind is negligible ($U \approx U_g$).

Since there is almost no surface precipitation at this time, PV gradient changes are expected to be governed mainly by $\delta\|\nabla_\theta PV\|_{\mathrm{ADI}}$, Equation (16). Indeed, adiabatic deformation and shear are responsible for almost all modification of $\|\nabla_\theta PV\|$ (Figure 5a,c), and $\delta\|\nabla_\theta PV\| \approx \delta\|\nabla_\theta PV\|_{\mathrm{ADI}}$ holds almost everywhere inside the jet streak. For grid points inside the jet streak with $\delta\|\nabla_\theta PV\| > 0.05$ PVU $\cdot(100\,\mathrm{km}\cdot 3\,\mathrm{hr})^{-1}$, the relative contributions by diabatic processes are less than 33% for nearly 80% of grid points and $|\delta\|\nabla_\theta PV\|_{\mathrm{DIA}}/\delta\|\nabla_\theta PV\||$ exceed 75% only about 1% of the time. The direct- and indirect-diabatic contributions to $\delta\|\nabla_\theta PV\|$ are both close to zero and counteract each other in the core of the jet streak (Figure 5d,e). Hence, the total diabatic contributions (Figure 5b) are negligible inside the jet streak.

Finally, we consider $\|\nabla_\theta \ln(PV)\|$. As predicted by theory, the band of high $\|\nabla_\theta \ln(PV)\|$ overlaps with the jet axis (Figure 3g), without the stratosphereward displacement observed for $\|\nabla_\theta PV\|$ (Figure 3d). The Lagrangian rate of change $\delta\|\nabla_\theta \ln(PV)\|$ is positive in the jet entrance region (brown in Figure 3i) and negative in the exit region (blue). There is no increase in $\delta\|\nabla_\theta \ln(PV)\|$ towards the stratospheric side of the jet, unlike for $\delta\|\nabla_\theta PV\|$ (Figure 3f). However, $\delta\|\nabla_\theta \ln(PV)\|$ is also dominated by dry dynamics (Figure 6c), with only small direct-diabatic contributions $\delta\|\nabla_\theta \ln(PV)\|_{\mathrm{DIA,DIR}}$ near the jet streak centre on its tropospheric side (brown in Figure 6d). This diabatic contribution is less evident in $\|\nabla_\theta PV\|$, which is a consequence of the normalisation of the PV gradient by PV in
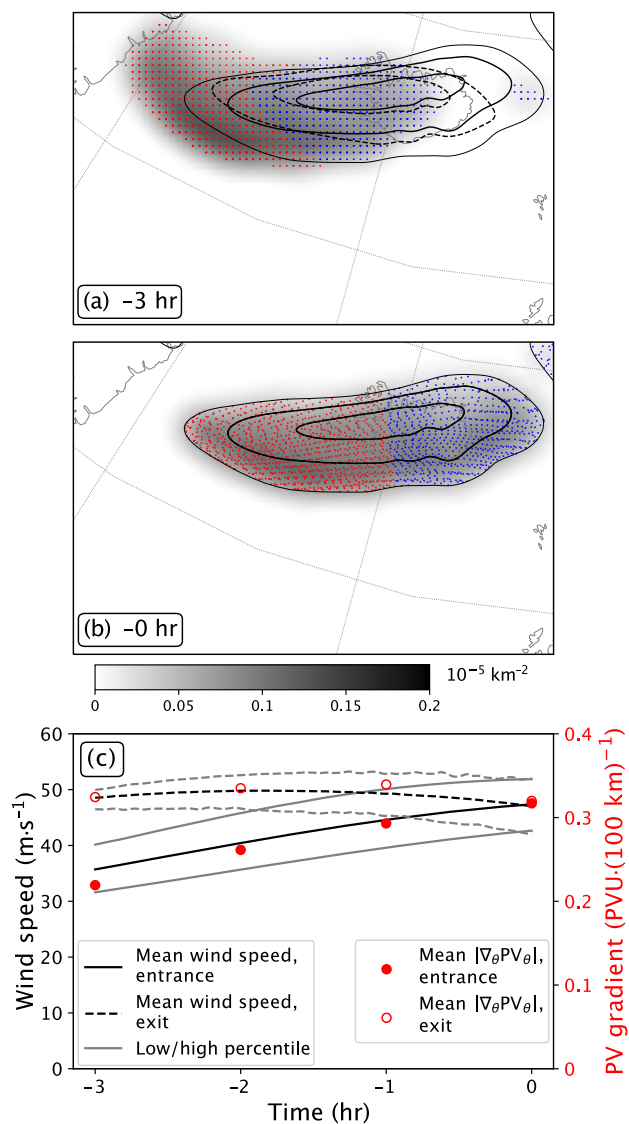

FIGURE 4 Changes along trajectories during the 3 hr before they enter a jet streak at 0600 UTC on September 22, 2016. (a, b) Shown are normalised density as grey shading and location as dots of the trajectories ending in the jet streak as defined by wind speed above 30 m·s⁻¹ at 320 K: (a) 3 hr before their arrival, and (b) upon their arrival. Black contours show horizontal wind speed at arrival time in solid and 3 hr earlier in dashed for 30, 40, and 50 m·s⁻¹. The dots are coloured red or blue according to whether a trajectory arrives in the entrance or exit region of the jet streak. (c) Black lines show the mean temporal evolution of wind speed along all trajectories ending in the jet streak as defined by wind speed above 40 m·s⁻¹ at 320 K, separated by whether they arrive in the jet entrance (solid lines) or exit (dashed) region, with grey lines indicating the 15th and 85th percentiles. Red dots show the mean $\|\nabla_\theta PV\|$ of trajectories arriving in the jet entrance (filled dots) and exit region (open). Note the different jet thresholds of (a, b) 30 m·s⁻¹, which was lowered for visualisation purposes, and (c) 40 m·s⁻¹, as in the rest of the study. PV: potential vorticity; PVU: PV units. [Colour figure can be viewed at wileyonlinelibrary.com]
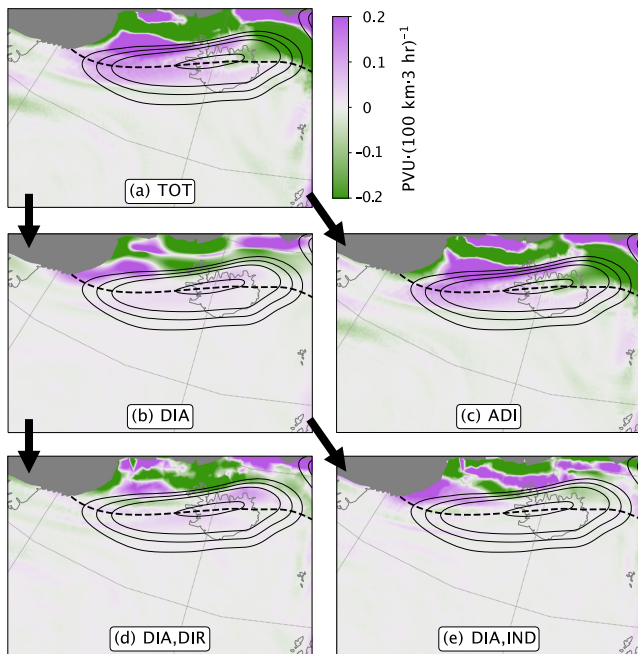
FIGURE 5 Lagrangian-based fields at 0600 UTC on September 22, 2016. Shown in colours are (a) difference between absolute and 3 h advected $\|\nabla_\theta PV\|$ at 320 K; 3 h $\delta\|\nabla_\theta PV\|$ due to (b) total diabatic contributions to $\delta\|\nabla_\theta PV\|$, (c) adiabatic deformation, (d) direct-diabatic contribution, and (e) indirect-diabatic contribution. Grey areas and black contours are as in Figure 3. PV: potential vorticity; PVU: PV units. [Colour figure can be viewed at wileyonlinelibrary.com]

$\delta\|\nabla_\theta \ln(PV)\|$, which compensates for the large absolute gradient changes in stratospheric high-PV regions.

This case study of an isolated, dry jet streak demonstrates the utility of the Lagrangian PV gradient framework in general, and of $\|\nabla_\theta PV\|$ and $\|\nabla_\theta \ln(PV)\|$ as insightful diagnostics in particular. Regions of high $\|\nabla_\theta \ln(PV)\|$ overlap the jet axis and represent the jet streak as a coherent dynamical unit better than $\|\nabla_\theta PV\|$ does, reducing the latter's overemphasis on changes in high-PV regions, such as the stratosphere. Though this makes $\|\nabla_\theta \ln(PV)\|$ better suited to represent the predominantly dry dynamics with only small diabatic contributions of this jet streak, the simpler $\|\nabla_\theta PV\|$ diagnostic yields qualitatively similar findings of deformation-dominated changes and a clear distinction between air parcels that experienced confluence or diffluence.

In the foregoing theoretical considerations, the significance of the PV gradient as a proxy for the flow field is based on several assumptions. A vertical cross-section through the Iceland jet streak (left in Figure 7) reveals a tropopause fold intersecting the jet core and a flow field that is fairly symmetric close to its centre with a slightly enhanced wind gradient on the stratospheric side (Figure 7a). A closer inspection of U, σ, and $\partial_y\sigma$ along

the 320 K isentrope, which intersects the maximum in wind speed (bold dashed contour in Figure 7a), reveals that (a) $|\frac{f_0}{\sigma_0}\partial_y\sigma'/\partial_y^2 U| \leq 0.011 \ll 1$, (b) $|\sigma'/\sigma_0| \leq 0.15 \ll 1$ throughout the entire jet region (Figure 7d), and (c) the wind speed gradient reaches the same order of magnitude as the Coriolis parameter on both side of the jet. The implication of (a) and (b) is that both $\|\nabla_\theta \ln(PV)\|$ and $\|\nabla_\theta PV\|$ are indicative of the wind speed. The locally strong wind speed gradient does not invalidate this relation, but leads to a broadening of the region of high $\|\nabla_\theta \ln(PV)\|$ towards the troposphere (blue line in Figure 7j).

4.3 | Case 2: *Vladiana* jet streak

The second case study focuses on a jet streak at 0000 UTC on September 23, 2016, associated with extratropical cyclone *Vladiana* ("B" in Figure 8a–c). A comparison of absolute and advective PV changes along air parcel trajectories ending in different regions of the jet streak indicates widespread PV creation on the stratospheric side of the jet axis (red in Figure 8c), PV destruction on its tropospheric side (blue), and yet another band of PV creation farther into the troposphere. The Lagrangian PV changes over the preceding 3 hr are larger than for the Iceland jet streak studied in the previous section. In particular, the substantial decrease in PV on the tropospheric side of the jet was not seen for that case, and surface precipitation in this case points to the relevance of moist diabatic processes in destroying PV (Figure 2e). The two aligned bands of negative and positive δPV on the tropospheric side of the jet axis are reminiscent of the PV dipoles formed by embedded convection in the rising WCB ahead of the cold front (Oertel *et al.*, 2019a). Closer inspection of the unfiltered field confirms that these bands indeed originate from isolated mesoscale PV dipoles above cold-frontal surface precipitation on the tropospheric side of the jet axis (not shown). The net circulation induced by the dipoles is directed against the jet stream at the centre of the elongated bands, causing wind speeds to locally drop below 30 m·s^{-1} (Figure 8a). At the same time, the negative PV band near the tropopause enhances $\|\nabla_\theta PV\|$ in the jet streak core, thus intensifying the jet, whereas the positive PV band induces along-jet flow on its tropospheric side, which broadens the jet. The strongest changes in $\|\nabla_\theta \ln(PV)\|$ comprise bands of alternating sign along the jet (Figure 8g) aligned with the elongated PV change dipoles. This illustrates the relevance of mesoscale features, whose representation is improved by high-resolution simulations with explicit convection (Done *et al.*, 2006; Clarke *et al.*, 2019; Oertel *et al.*, 2019a), on the development of synoptic-scale features like jet streaks.

FIGURE 6   Lagrangian-based fields at 0600 UTC on September 22, 2016. Shown in colours are (a) difference between absolute and 3 h advected $\|\nabla_\theta \ln(PV)\|$; 3 h $\delta\|\nabla_\theta \ln(PV)\|$ due to (b) total diabatic contributions to $\delta\|\nabla_\theta \ln(PV)\|$, (c) adiabatic deformation, (d) direct-diabatic contribution, and (e) indirect-diabatic contribution. Grey areas and black contours are as in Figure 3. PV: potential vorticity; PVU: PV units. [Colour figure can be viewed at wileyonlinelibrary.com]
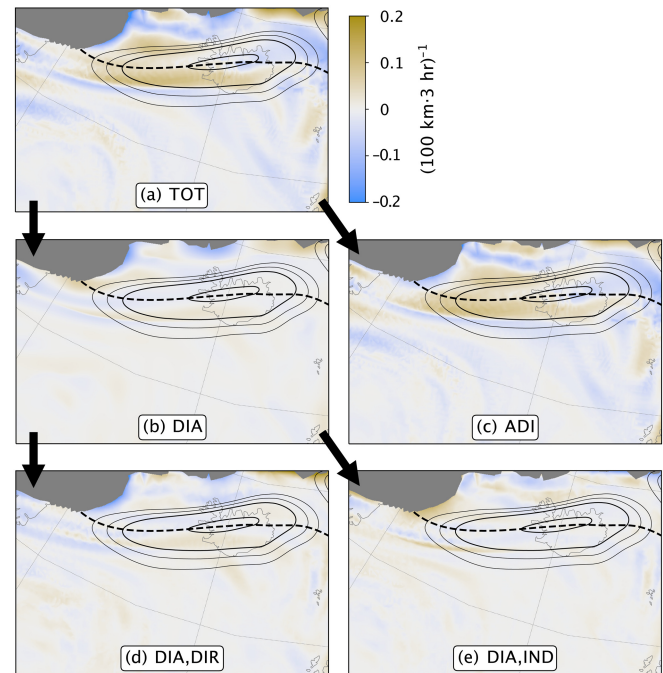
We begin our analysis of $\|\nabla_\theta PV\|$ by noting that, for the still existing Iceland jet streak (now "A2" in Figure 8a–c), both the magnitude and the stratosphereward displacement of $\|\nabla_\theta PV\|$ decreased as the jet broadened. These changes are consistent with theory, as a wider jet implies a lower wave number and a smaller curvature of the horizontal wind speed on an isentropic surface for a given maximum wind speed, Equation (12). For the *Vladiana* jet, the Lagrangian change $\delta\|\nabla_\theta PV\|$ shows a widespread increase throughout the jet stream, except for small reductions on the tropospheric side of the jet axis near the aforementioned PV dipole bands and on the stratospheric side of the jet axis (Figure 8f). The lack of a distinct entrance and exit pattern, as was observed in the Iceland case, indicates that the jet streak as a whole is growing. Mean wind speed increased not only along parcel trajectories ending in the jet streak entrance (solid lines in Figure 9c) but also along those ending in the jet exit (dashed). Note that the ratio between increases in $\|\nabla_\theta PV\|$ and wind speed is higher for air parcels at the exit of the *Vladiana* jet (Figure 9c) than for those at the entrance of the Iceland jet (Figure 9d). A possible explanation is that the smaller width of the *Vladiana* jet streak leads to a larger wind speed curvature, and hence stronger overall PV gradients. Alternatively, the flow might not be in geostrophic balance during the intensification of the *Vladiana* jet streak, which implies $U_g > U$; that is, air parcel acceleration lags behind PV gradient increase for those air parcels, making them slower than indicated by PV gradients. Additionally, for air parcels in the region of PV dipoles that are associated with convective outflow, variations in σ significantly contribute to the PV gradient, as we find in Figure 7e. This is discussed in detail at the end of this section.

The decomposition of $\delta\|\nabla_\theta PV\|$ into adiabatic and diabatic contributions highlights the differences of this dynamic situation compared with the Iceland case (Figure 10c–e). Air parcels that end in the *Vladiana* jet streak are strongly influenced by diabatic processes (Figure 8c). The adiabatic contributions decreased $\|\nabla_\theta PV\|$ on the tropospheric side of the jet axis (green in Figure 10b) and increased it in the jet core (purple). Adiabatic changes thus make the jet narrower and stronger. However, on the tropospheric side of the jet axis, direct- and indirect-diabatic processes overall increased $\|\nabla_\theta PV\|$ (purple in Figure 10d,e), especially near the edge of the jet, where $\|\nabla_\theta PV\|$ decreased only in small areas despite the negative adiabatic contributions. Indeed, diabatic contributions increased the PV gradient along most air parcel trajectories, with a decrease only along about one in seven trajectories ending in the jet streak, or about 14%. In regions with $\delta\|\nabla_\theta PV\| > 0.05\,$PVU $\cdot(100\,\text{km}\cdot 3\,\text{hr})^{-1}$, diabatic contributions are comparable in magnitude to adiabatic contributions. Specifically, the relative diabatic contribution $|\delta\|\nabla_\theta PV\|_{DIA}/\delta\|\nabla_\theta PV\||$ exceeds 33% for
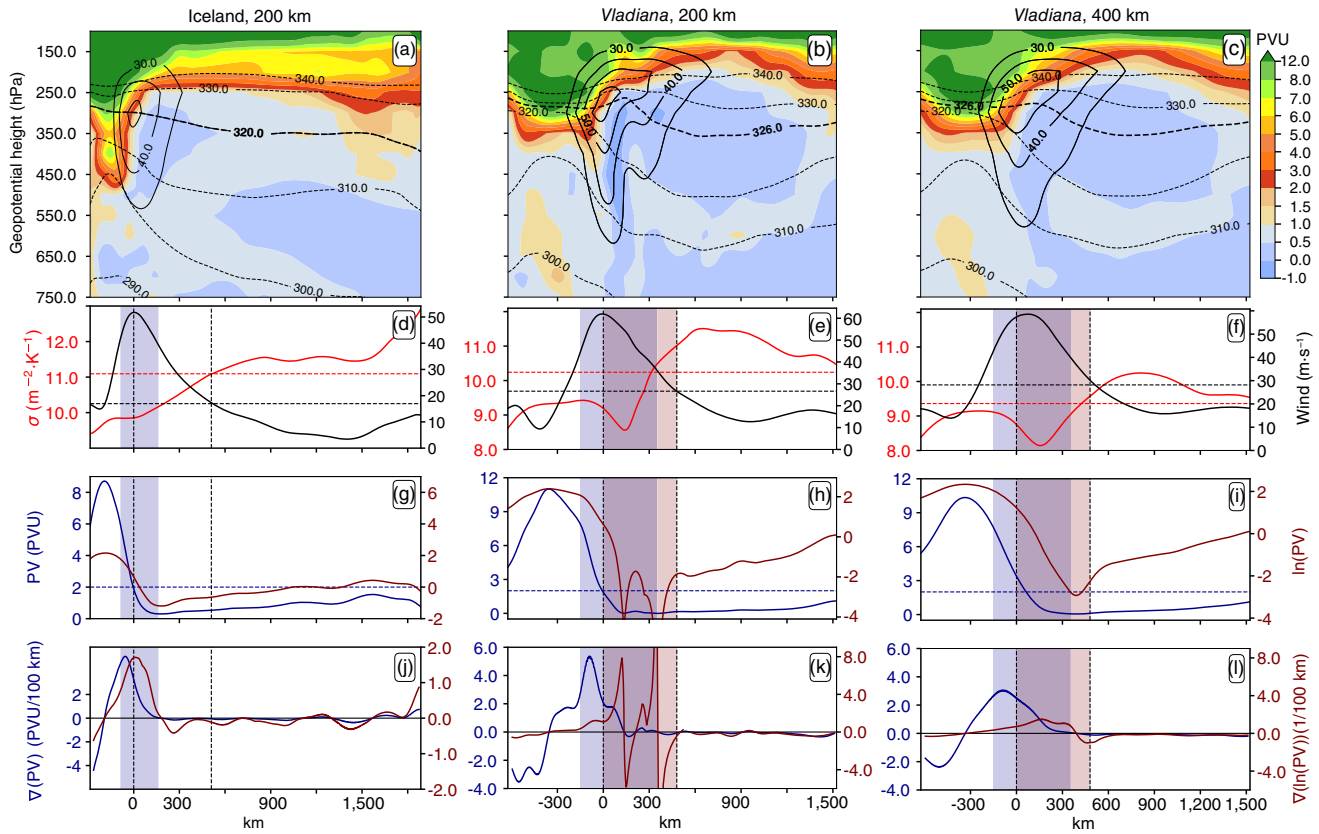
FIGURE 7 Vertical cross sections through (left) the Iceland jet streak at 0600 UTC on 22 September 2016 (see Figure 2d) and (centre and right) the Vladiana jet streak at 0000 UTC on 23 September 2016 (see Figure 2e). All fields have been low-pass filtered with a filter length of (left and centre) 200 km and (right) 400 km. (a–c) The cross-sections show PV in colours, horizontal wind speed as solid contours and selected isentropes as dashed contours with the isentrope intersecting the jet streak centre highlighted in bold. The position of maximum wind speed in the cross section is defined as the jet streak center. (d–l) The line plots show selected variables along these isentropes: (d–f) stratification in red and wind speed in black, (g–i) PV in blue and ln PV in brown, (j–l) $+\theta$PV in blue and $+\theta$ (ln PV) in brown. The dashed horizontal lines depict (d–f) the mean of the respective variable along the cross-section and (g–i) the 2 PVU dynamical tropopause. Vertical lines in show the position where wind speed equals its maximum (at 0 km) and mean. The shaded regions indicate in blue the jet streak region (wind speed) 40 ms^{-1}, and in red areas where the validity of the assumptions made in Section 2.1 are violated (i.e., $\zeta \geq f_0$ and/or $|\frac{f_0}{\sigma_0}\partial_y\sigma'| \geq |\partial_y^2 U|$). In those areas, PV gradients merely relate to strong changes in both the flow field and the stratification rather than being a direct proxy for the wind speed. [Colour figure can be viewed at wileyonlinelibrary.com]

70% of the grid points inside jet streak B, and for 23% of the grid points it even exceeds 75%, a pronounced contrast to the jet streak A1, where it is only about 1%. Diabatic processes thus tend to amplify and broaden the *Vladiana* jet streak. This acts to reinforce adiabatic tendencies in some regions, such as in the jet core, while countering the influence of adiabatic processes in others, like on the tropospheric side of the jet above the surface precipitation band. The increase in $\|\nabla_\theta \mathrm{PV}\|$ in the jet core region is caused by direct-diabatic processes, whereas that above the surface precipitation is due to a combination of direct- and indirect-diabatic processes that cause a broadening of the jet in that region. Finally, we find that changes on the stratospheric side of the jet are generally dominated by adiabatic processes, even though previous studies found substantial diabatic PV modification by radiation and turbulence in that area (Gray, 2006; Spreitzer *et al.*, 2019b).

This discrepancy can be partially explained by radiation effects being negligible over time periods as short as 3 hr but becoming relevant on longer time-scales. The absence of turbulent effects might be a consequence of the much higher spatial resolution of our COSMO simulation (1.1 km) compared with previous studies (18 km in Spreitzer *et al.*, 2019b; 60 km in Gray, 2006), causing a considerable fraction of the subgrid turbulence contributing to diabatic PV modifications in those studies to be resolved explicitly by our model.

Contrary to what is found for the Iceland jet, the peak in $\|\nabla_\theta \ln(\mathrm{PV})\|$ is not overlapping with the jet axis; rather, it exhibits a tropesphereward displacement. This is explained by the strong variability in stratification on the tropospheric side of the jet in this case, which dominates $\|\nabla_\theta \ln(\mathrm{PV})\|$ in this region, as we will discuss at the end of this section. Though this means that a direct link to
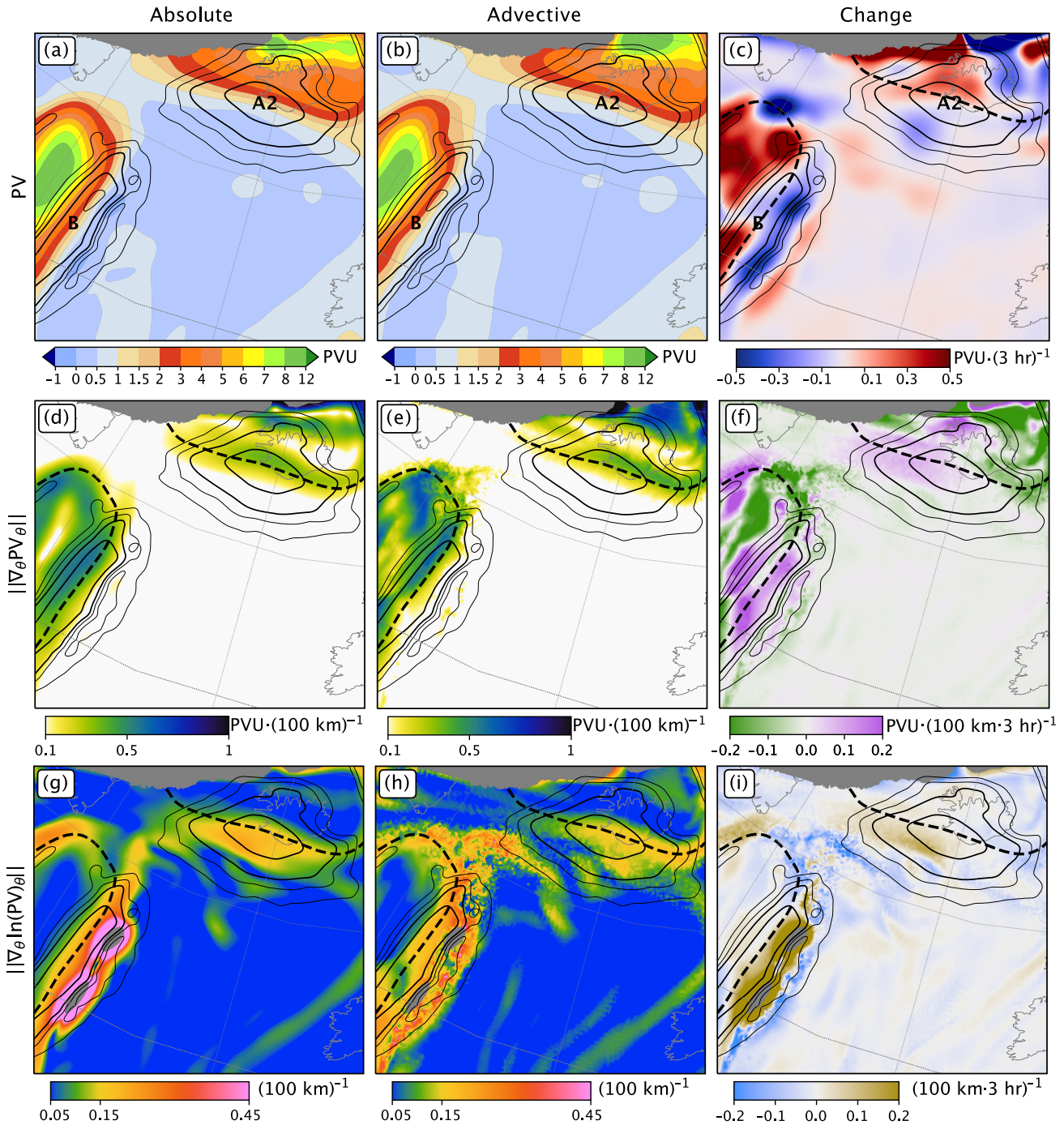
FIGURE 8 Similar to Figure 3, but for jet streaks A2 and B at 0000 UTC on September 23, 2016. Note again that only a part of the whole domain is shown (see Figure 1). PV: potential vorticity; PVU: PV units. [Colour figure can be viewed at wileyonlinelibrary.com]

the wind speed is not given here, large $\|\nabla_\theta \ln(PV)\|$ on the tropospheric side of the jet axis pinpoints regions where the thermal wind balance and increasing stability lead to a broadening of the jet. These are still dynamically interesting regions. We find the strongest changes in $\|\nabla_\theta \ln(PV)\|$ on the tropospheric side of the jet, where it is largely positive in the regions where $\|\nabla_\theta \ln(PV)\|$ is well defined. The decomposition into the different components reveals that $\delta\|\nabla_\theta \ln(PV)\|_{DIA,DIR}$ and $\delta\|\nabla_\theta \ln(PV)\|_{DIA,IND}$

are of similar magnitude to $\delta\|\nabla_\theta \ln(PV)\|_{ADI}$ and enhance each other in some regions but partially offset each other elsewhere. A comparison of the three components (Figure 11c–e) with the total change $\delta\|\nabla_\theta \ln(PV)\|$ (Figure 11a) reveals that adiabatic deformation on its own cannot explain $\delta\|\nabla_\theta \ln(PV)\|$ even qualitatively, especially on the tropospheric side of the jet. Direct-diabatic changes are crucial alongside dry deformation to explain the increase in $\|\nabla_\theta \ln(PV)\|$ in the jet core, especially on the
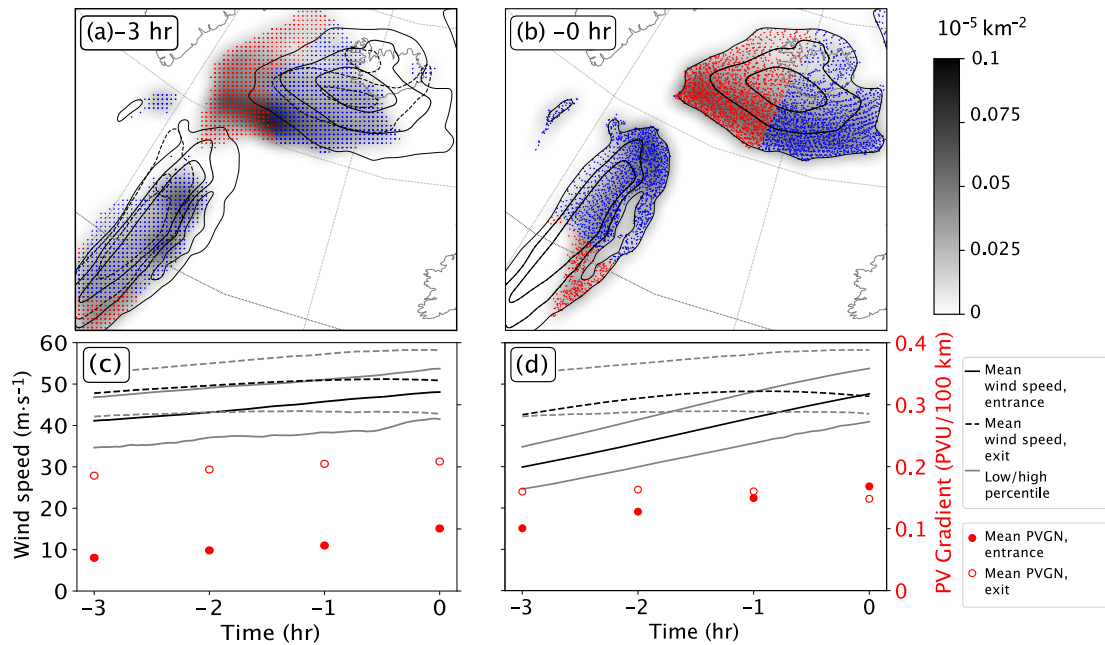
FIGURE 9   Similar to Figure 4, but for trajectories ending in the jet at 0000 UTC on September 23, 2016. The line plots show (c) *Vladiana* jet trajectories (bottom left in a, b) and (d) Iceland jet trajectories (top right). Note again the different jet thresholds of (a, b) 30 m·s^{-1} (visualisation purposes) and (c, d) 40 m·s^{-1} (the rest of the study). PVGN: potential vorticity gradient; PVU: potential vorticity units. [Colour figure can be viewed at wileyonlinelibrary.com]

tropospheric side of the jet axis. Adiabatic deformation acts to reduce the PV gradient on the tropospheric side of the jet, whereas indirect-diabatic processes act to enhance it.

In summary, the temporal evolution of the *Vladiana* jet streak is characterised equally by adiabatic and diabatic processes. Adiabatic processes tend to amplify the PV gradient, which intensifies and narrows the jet. Direct-diabatic PV gradient modification acts in the same direction by intensifying the PV gradient in the jet core, especially on the tropospheric side of the jet. However, the influence of indirect-diabatic processes is substantial and of opposite sign in the jet core. Comparing $\|\nabla_\theta PV\|$ and $\|\nabla_\theta \ln(PV)\|$ reveals that the latter emphasises processes that take place in the troposphere and near the tropopause. Because the large absolute gradient changes in the stratosphere are primarily adiabatic, the fact that they are de-emphasised by the normalisation in $\delta\|\nabla_\theta \ln(PV)\|$ emphasises diabatic contributions compared with $\delta\|\nabla_\theta PV\|$.

The vertical cross-sections through the *Vladiana* jet streak (centre and right in Figure 7) show a meridionally wider jet streak above 320 K than in the Iceland case that also extends to lower altitudes. PV dipoles with regions of negative PV prevail even after applying a 200 km low-pass filter, indicating that the assumption of a small perturbation of the field is locally not well justified and that ln PV is thus not well defined in these small regions (Figure 7h). Figure 7e shows that the assumption of low-variability stability close to the jet core is violated with $|\frac{f_0}{\sigma_0}\partial_y\sigma'/\partial_y^2 U|$

locally exceeding 10. Applying a low-pass filter with a larger wavelength removes the regions of negative PV, but the strong variations in σ remain (Figure 7c,f,i,l). In such a situation, the PV gradient is indicative of jet regions where variations in thermal stratification (here due to diabatic processes) matter as much as variations in the flow field.

5 | CONCLUSIONS

In this study, we outline a novel Lagrangian-based PV gradient framework that allows for disentangling the effects of adiabatic and diabatic processes on the evolution PV gradients. Central to the diagnostic is the relationship between the wind speed, its curvature, and elongated bands of enhanced PV gradients (Davies, 1981; Davies and Rossa, 1998; Martius *et al.*, 2010), which enables the study of jet dynamics using the PV gradient as a proxy for the flow field. The first part of this study reflects the intention of quantitatively connecting the gradient of PV to the flow field. To summarise:

- The assumptions that allow for establishing a quantitative link between $\|\nabla_\theta PV\|$ or $\|\nabla_\theta \ln(PV)\|$ and the flow field require relatively low variability in stratification along tropopause-intersecting isentropic surfaces and sufficiently broad jets. If this is not the case, regions with high PV gradients still serve as proxy for a jet. In
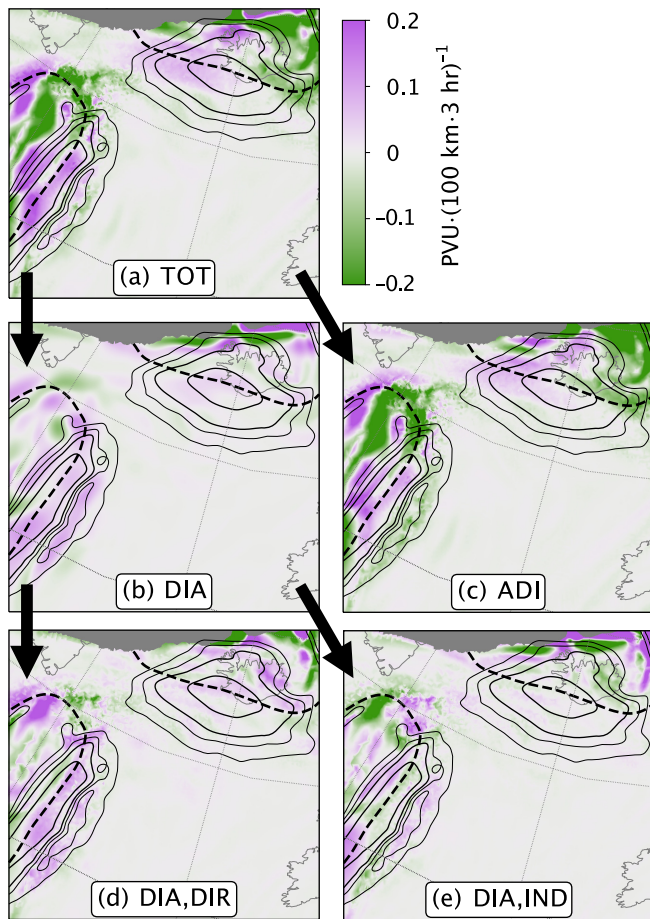
FIGURE 10 Similar to Figure 5, but for jet streaks A2 and B at 0000 UTC on September 23, 2016. PVU: potential vorticity units. [Colour figure can be viewed at wileyonlinelibrary.com]

this case, the nature of the jet is best described as a region of increased wind speed and notable changes in stratification.

- Owing to the meridional variation in stratification across the tropopause, PV gradients tend to reside on the stratospheric side of the jet axis, whereas large values of $\|\nabla_\theta \ln(PV)\|$ exhibit a slight troposphereward displacement as a result of variations in vorticity. In general, $\|\nabla_\theta \ln(PV)\|$ shows a higher degree of alignment with the jet axis than $\|\nabla_\theta PV\|$ does.

The derived relationship between the curvature of the flow and the gradient of ln(PV) points towards a potential connection with the dynamics of Rossby waves, whose dispersion relation depends on wind speed curvature. To explore this connection in detail, further investigation into its theoretical underpinnings is warranted in future studies.

In the second part of this study, the PV gradient framework is applied as a diagnostic tool to disentangle adiabatic and diabatic contributions to the evolution of two jet streaks over the eastern North Atlantic by investigating the
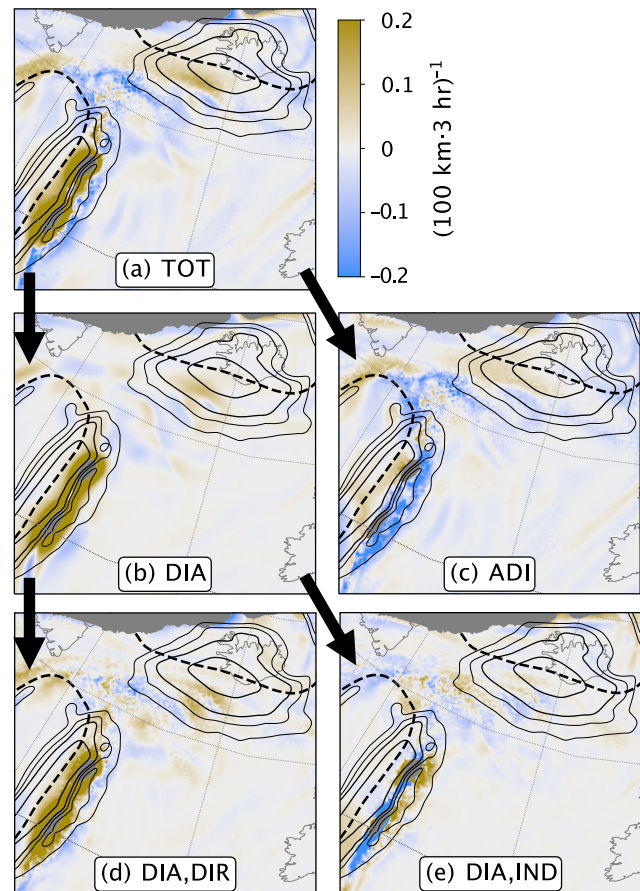

FIGURE 11 Similar to Figure 6, but for jet streaks A2 and B at 0000 UTC on September 23, 2016. [Colour figure can be viewed at wileyonlinelibrary.com]

material derivative of the corresponding PV gradient tendencies along air parcel trajectories. A suitable low-pass filter in space is applied to the PV fields to ensure adherence to the scaling assumptions underlying the links between the flow field and both $\|\nabla_\theta \ln(PV)\|$ and $\|\nabla_\theta PV\|$ that we derived in the first part of this study.

The first jet streak on September 22, 2016, is located southwest of Iceland and forms a zonally oriented, nearly stationary flow feature not accompanied by a surface cyclone. It is part of a larger anticyclonically breaking Rossby wave characterised by the formation of a meridionally extended PV streamer farther downstream over the British Isles. The second jet streak, on September 23, 2016, is associated with the mature extratropical cyclone *Vladiana* located in the central North Atlantic. This jet streak is aligned with a strong WCB rising along the surface cold front to upper levels. To summarise the key results of the two case studies:

- Dry deformation and shear drive the evolution of the Iceland jet streak. Air parcels traversing it do not experience significant diabatic PV gradient changes, except in a small region in the left jet exit.

- Pronounced diabatic processes contribute to the Lagrangian PV-gradient tendencies along air parcels ending in the jet streak associated with cyclone *Vladiana*. The direct-diabatic contributions, which denote PV gradient changes resulting solely from diabatic PV modification, tend to accelerate the jet, whereas indirect-diabatic contributions resulting from deformation acting on diabatically modified PV tend to decrease the PV gradient, in particular close to the jet centre.

- Dry deformation causes a reduction in the PV gradient, especially (and as expected) near the exit of the *Vladiana* jet streak, but the negative deformation-driven PV gradient tendency is almost everywhere offset by diabatic build-up of PV gradients.

The Iceland case study highlights that jet streaks can be sustained in absence of diabatic processes, in which case the PV gradient evolution is akin to adiabatic PV frontogenesis (Davies and Rossa, 1998). The *Vladiana* case study illustrates the pronounced impact of diabatic processes on the intensification of a jet streak and the associated PV gradient, including a separation into direct- and indirect-diabatic contributions. Furthermore, mesoscale PV dipoles caused by embedded convection in the WCB (e.g., Oertel *et al.*, 2019a) that modify the jet at the synoptic scale illustrate the utility of kilometre-scale convection-permitting simulations even for studies focusing on the large-scale circulation. These are mostly seen as indirect-diabatic contributions to the PV gradient changes because this PV non-conservation occurs in a region of high shear. Direct-diabatic contributions are found more towards the centre of the jet streak, where the shear is low. Decomposing the diabatic PV gradient tendency further into individual diabatic processes (which we already implemented in the COSMO model) is left to future studies, as is an extension of the trajectories analysis time window to more than 3 hr, which is limited in this study by the size of the computation domain. We also analysed Eulerian PV-frontogenesis for both case studies, and a figure showing the result of this analysis for the *Vladiana* case study can be found in Supporting Information Section S3, Figure S1.

5.1 | Caveats and further considerations

The key limitation of the PV gradient framework is the scale separation required to link wind speed to the PV gradient, which is based on a linearisation around a mean flow at rest and on the assumption that stratification varies smoothly close to the jet centre. The latter assumption can be violated in the presence of strong tropopause folds, which often accompany intense jets. Here, we use a low-pass Fourier filter with a cut-off wavelength of 200 km. Other methods have been proposed to link mesoscale PV anomalies and PV gradients to a wind field (Oertel and Schemm, 2021). However, although our framework does not represent the effects of mesoscale PV anomalies directly, the mesoscale PV dipoles that modify the large-scale flow in the *Vladiana* case illustrate that the link to wind anomalies is well captured even after filtering the kilometre-scale data.

Despite these caveats, this study demonstrates how to exploit the advantages of kilometre-scale simulations for understanding large-scale dynamics by sufficiently filtering the high-resolution fields to ensure the overall applicability of large-scale concepts. As the next generation of climate models approach kilometre-scale grid spacing, it becomes increasingly necessary to find ways to apply large-scale concepts to high-resolution data, which, as demonstrated here, is possible with careful consideration of the assumptions underlying the theory. However, the framework itself is agnostic about model resolution and also applicable to coarser datasets, such as current-generation reanalyses or global model simulation output. Subsequent studies in this area could show its merits on larger scales.

5.2 | Outlook

Our study can only be considered a first step towards a more systematic and long-term analysis of jet dynamics from a PV gradient perspective in present and future climates. Of particular interest are changes in the PV gradient at the tropopause and related jet properties in a warmer atmosphere, in which the relative importance of diabatic processes potentially increases, as well as trends in the properties of Rossby wave propagation resulting from such changes. Furthermore, the PV gradient framework appears well suited to investigate the reported increase in the strength of extreme jet streaks over the North Atlantic (Simmons, 2022). As a next step, we envision an investigation of the PV gradient evolution from a perspective following a jet streak using a natural coordinate system rather than the traversing air parcels because "the individual streaks tend to progress along the current; however, they move very much slower than the wind" (Palmén and Newton, 1969, p. 207).

AUTHOR CONTRIBUTIONS

Mona Bukenberger: conceptualization; investigation; visualization; writing – original draft; writing – review and editing. **Stefan Rüdisühli:** data curation; visualization;

CONFLICT OF INTEREST STATEMENT
The authors declare no conflict of interest.

ORCID
Mona Bukenberger 🄳 https://orcid.org/0000-0002-0171-2996
Stefan Rüdisühli 🄳 https://orcid.org/0000-0003-1582-1138
Sebastian Schemm 🄳 https://orcid.org/0000-0002-1601-5683

REFERENCES
Ahmadi-Givi, F., Graig, G.C. and Plant, R.S. (2004) The dynamics of a midlatitude cyclone with very strong latent-heat release. *Quarterly Journal of the Royal Meteorological Society*, 130, 295–323.

Appenzeller, C. and Davies, H.C. (1996) PV morphology of a frontal-wave development. *Meteorology and Atmospheric Physics*, 58, 21–40.

Archambault, H.M., Bosart, L.F., Keyser, D. and Cordeira, J.M. (2013) A climatological analysis of the extratropical flow response to recurving western north pacific tropical cyclones. *Monthly Weather Review*, 141, 2325–2346.

Archambault, H.M., Keyser, D., Bosart, L.F., Davis, C.A. and Cordeira, J.M. (2015) A composite perspective of the extratropical flow response to recurving western north pacific tropical cyclones. *Monthly Weather Review*, 143, 1122–1141.

Attinger, R., Spreitzer, E., Boettcher, M., Forbes, R., Wernli, H. and Joos, H. (2019) Quantifying the role of individual diabatic processes for the formation of PV anomalies in a North Pacific cyclone. *Quarterly Journal of the Royal Meteorological Society*, 145, 2454–2476.

Attinger, R., Spreitzer, E., Boettcher, M., Wernli, H. and Joos, H. (2021) Systematic assessment of the diabatic processes that modify low-level potential vorticity in extratropical cyclones. *Weather and Climate Dynamics*, 2, 1073–1091.

Barnes, E.A. and Screen, J.A. (2015) The impact of arctic warming on the midlatitude jet-stream: can it? Has it? Will it? *WIREs Climate Change*, 6, 277–286.

Binder, H., Boettcher, M., Joos, H. and Wernli, H. (2016) The role of warm conveyor belts for the intensification of extratropical cyclones in northern hemisphere winter. *Journal of the Atmospheric Sciences*, 73, 3997–4020.

Bishop, C.H. and Thorpe, A.J. (1994) Potential vorticity and the electrostatics analogy: quasi-geostrophic theory. *Quarterly Journal of the Royal Meteorological Society*, 120, 713–731.

Bjerknes, J. and Solberg, H. (1922) Life cycle of cyclones and the polar front theory of atmospheric circulation. *Geophysics Publik*, 3, 1–18.

Boyle, J.S. and Bosart, L.F. (1986) Cyclone–anticyclone couplets over North America. Part II: analysis of a major cyclone event over the eastern United States. *Monthly Weather Review*, 114, 2432–2465.

Branstator, G. and Teng, H. (2017) Tropospheric waveguide teleconnections and their seasonality. *Journal of the Atmospheric Sciences*, 74, 1513–1532.

C2SM. (2020) Following the air on GPUs. *C2SM Newsletter*, 2020.11. https://c2sm.ethz.ch/news/archive/2020/11/following-the-air-on-gpus.html.

Čampa, J. and Wernli, H. (2012) A PV perspective on the vertical structure of mature midlatitude cyclones in the northern hemisphere. *Journal of the Atmospheric Sciences*, 69, 725–740.

Chagnon, J.M. and Gray, S.L. (2015) A diabatically generated potential vorticity structure near the extratropical tropopause in three simulated extratropical cyclones. *Monthly Weather Review*, 143, 2337–2347.

Chagnon, J.M., Gray, S.L. and Methven, J. (2013) Diabatic processes modifying potential vorticity in a North Atlantic cyclone. *Quarterly Journal of the Royal Meteorological Society*, 139, 1270–1282.

Clarke, S.J., Gray, S.L. and Roberts, N.M. (2019) Downstream influence of mesoscale convective systems. Part 1: influence on forecast evolution. *Quarterly Journal of the Royal Meteorological Society*, 145, 2933–2952.

COSMO. (2022) Concortium for small-scale Modeling. https://www.cosmo-model.org.

Crezee, B., Joos, H. and Wernli, H. (2017) The microphysical building blocks of low-level potential vorticity anomalies in an idealized extratropical cyclone. *Journal of the Atmospheric Sciences*, 74, 1403–1416.

CSCS. (2022) Piz Daint at the Swiss National Supercomputing Centre. https://www.cscs.ch/computers/piz-daint/.

Dacre, H.F. and Gray, S.L. (2006) Life-cycle simulations of shallow frontal waves and the impact of deformation strain. *Quarterly Journal of the Royal Meteorological Society*, 132, 2171–2190.

Davies, H. (1997) Emergence of the mainstream cyclogenesis theories. *Meteorologische Zeitschrift*, 6, 261–274.

Davies, H., Schär, C. and Wernli, H. (1991) The palette of fronts and cyclones within a baroclinic wave development. *Journal of the Atmospheric Sciences*, 48, 1666–1689.

Davies, H.C. (1981) An interpretations of sudden warmings in terms of potential vorticity. *Journal of the Atmospheric Sciences*, 38, 427–445.

Davies, H.C. and Didone, M. (2013) Diagnosis and dynamics of forecast error growth. *Monthly Weather Review*, 141, 2483–2501.

Davies, H.C. and Rossa, A.M. (1998) PV frontogenesis and upper-tropospheric fronts. *Monthly Weather Review*, 126, 1528–1539.

Davis, C.A. and Emanuel, K.A. (1991) Potential vorticity diagnostics of cyclogenesis. *Monthly Weather Review*, 119, 1929–1953.

Davis, C.A., Stoelinga, M.T. and Kuo, Y.-H. (1993) The integrated effect of condensation in numerical simulations of extratropical cyclogenesis. *Monthly Weather Review*, 121, 2309–2330.

Doms, G. and Schättler, U. (1999) The nonhydrostatic limited-area model lm (lokal-modell of the DWD. Part i: scientific documentation. Tech. Rep., German weather service (DWD), Offenbach, Germany. https://www.cosmo-model.org.

Done, J.M., Craig, G.C., Gray, S.L., Clark, P.A. and Gray, M.E.B. (2006) Mesoscale simulations of organized convection: importance of convective equilibrium. *Quarterly Journal of the Royal Meteorological Society*, 132, 737–756.

ECMWF. (2022a) European Centre for Medium-Range Weather Forecasts. https://www.ecmwf.int/en/about.

ECMWF. (2022b) IFS documentation. https://www.ecmwf.int/en/publications/ifs-documentation.

ECMWF. (2022c) Atmospheric model high resolution 10-day forecast (set I-HRES). https://www.ecmwf.int/en/forecasts/datasets/set-i.

Ertel, H. and Rossby, C.G. (1949) A new conservation-theorem of hydrodynamics. *Geofisica pura e applicata*, 14, 89–193.

Exner, F.M. (1925) *Dynamische Meteorologie*. Berlin, Heidelberg: Verlag Julius Springer, pp. 211–415.

Fehlmann, R. and Davies, H.C. (1999) Role of salient potential-vorticity elements in an event of frontal-wave cyclogenesis. *Quarterly Journal of the Royal Meteorological Society*, 125, 1801–1824.

Francis, J.A. and Vavrus, S.J. (2015) Evidence for a wavier jet stream in response to rapid Arctic warming. *Environmental Research Letters*, 10, 014005.

Fuhrer, O., Chadha, T., Hoefler, T., Kwasniewski, G., Lapillonne, X., Leutwyler, D., Lüthi, D., Osuna, C., Schär, C., Schulthess, T.C. and Vogt, H. (2018) Near-global climate simulation at 1 km resolution: establishing a performance baseline on 4888 GPUs with COSMO 5.0. *Geoscientific Model Development*, 11, 1665–1681.

Fuhrer, O., Osuna, C., Lapillonne, X., Gysi, T., Cumming, B., Bianco, M., Arteaga, A. and Schulthess, T.C. (2014) Towards a performance portable, architecture agnostic implementation strategy for weather and climate models. *Supercomputing Frontiers and Innovations*, 1, 45–62.

Grams, C.M. and Wernli, E.A. (2011) The key role of diabatic processes in modifying the upper-tropospheric wave guide: a North Atlantic case-study. *Quarterly Journal of the Royal Meteorological Society*, 137, 2174–2193.

Gray, S.L. (2006) Mechanisms of midlatitude cross-tropopause transport using a potential vorticity budget approach. *Journal of Geophysical Research: Atmospheres*, 111, D17113. https://agupubs.onlinelibrary.wiley.com/doi/abs/10.1029/2005JD006259

Gray, S.L., Dunning, C., Methven, J., Masato, G. and Chagnon, J.M. (2014) Systematic model forecast error in Rossby wave structure. *Geophysical Research Letters*, 41, 2979–2987.

Gyakum, J.R. (1983a) On the evolution of the QE II storm. I: synoptic aspects. *Monthly Weather Review*, 111, 1137–1155.

Gyakum, J.R. (1983b) On the evolution of the QE II storm. II: dynamic and thermodynamic structure. *Monthly Weather Review*, 111, 1156–1173.

Harnik, N. and Chang, E.K.M. (2004) The effects of variations in jet width on the growth of baroclinic waves: implications for mid-winter pacific storm track variability. *Journal of the Atmospheric Sciences*, 61, 23–40.

Harvey, B.J., Methven, J. and Ambaum, M.H.P. (2016) Rossby wave propagation on potential vorticity fronts with finite width. *Journal of Fluid Mechanics*, 794, 775–797.

Hoskins, B. and Berrisford, P. (1988) A potential vorticity perspective of the storm of 15–16 October 1987. *Weather*, 43, 122–129.

Hoskins, B.J., McIntyre, M.E. and Robertson, A.W. (1985) On the use and significance of isentropic potential vorticity maps. *Quarterly Journal of the Royal Meteorological Society*, 111, 877–946.

James, I.N. (1995) *Introduction to Circulating Atmospheres*. Cambridge: Cambridge University Press, pp. 171–180.

Joly, A. and Thorpe, A.J. (1990) Frontal instability generated by tropospheric potential vorticity anomalies. *Quarterly Journal of the Royal Meteorological Society*, 116, 525–560.

Kleinschmidt, E. (1955) Die Entstehung einer Höhenzyklone über Nordamerika. *Tellus*, 7, 96–110.

Kuo, Y.-H., Shapiro, M.A. and Donall, E.G. (1991) The interaction between baroclinic and diabatic processes in a numerical simulation of a rapidly intensifying extratropical marine cyclone. *Monthly Weather Review*, 119, 368–384.

Lapillonne, X. and Fuhrer, O. (2014) Using compiler directives to port large scientific applications to gpus: an example from atmospheric science. *Parallel Processing Letters*, 24, 1450003.

Lapillonne, X., Fuhrer, O., Spörri, P., Osuna, C., Walser, A., Arteaga, A., Gysi, T., Rüdisühli, S., Osterried, K. and Schulthess, T. (2016) Operational numerical weather prediction on a GPU-accelerated cluster supercomputer. In *EGU general assembly conference abstracts. Vol. 18 of EGU general assembly conference abstracts.*, EPSC2016–13554.

Manola, I., Selten, F., de Vries, H. and Hazeleger, W. (2013) "Waveguidability" of idealized jets. *Journal of Geophysical Research: Atmospheres*, 118, 10432–10440.

Martin, J.E. (2021) Recent trends in the waviness of the northern hemisphere wintertime polar and subtropical jets. *Journal of Geophysical Research: Atmospheres*, 126, e2020JD033668.

Martínez-Alvarado, O., Madonna, E., Gray, S.L. and Joos, H. (2016) A route to systematic error in forecasts of rossby waves. *Quarterly Journal of the Royal Meteorological Society*, 142, 196–210.

Martius, O., Schwierz, C. and Davies, H.C. (2010) Tropopause-level waveguid. *Journal of the Atmospheric Sciences*, 67, 866–879.

Methven, J. (2015) Potential vorticity in warm conveyor belt outflow. *Quarterly Journal of the Royal Meteorological Society*, 141, 1065–1071.

Miltenberger, A.K., Pfahl, S. and Wernli, H. (2013) An online trajectory module (version 1.0) for the nonhydrostatic numerical weather prediction model cosmo. *Geoscientific Model Development*, 6, 1989–2004.

Oertel, A., Boettcher, M., Joos, H., Sprenger, M., Konow, H., Hagen, M. and Wernli, H. (2019a) Convective activity in an extratropical cyclone and its warm conveyor belt — a case-study combining observations and a convection-permitting model simulation. *Quarterly Journal of the Royal Metereological Society*, 145, 1406–1426.

Oertel, A., Boettcher, M., Joos, H., Sprenger, M. and Wernli, H. (2019b) *Potential Vorticity Structure of Embedded Convection in a Warm Conveyor Belt and its Relevance for Large-Scale Dynamics*, 1, 127–153.

Oertel, A. and Schemm, S. (2021) Quantifying the circulation induced by convective clouds in kilometer-scale simulations. *Quarterly Journal of the Royal Meteorological Society*, 147, 1752–1766.

Palmén, E.H. and Newton, C.W. (1969) *Atmospheric Circulation Systems: Their Structure and Physical Interpretation*, Vol. 13. Academic press.

Pfahl, S., Schwierz, C., Croci-Maspoli, M., Grams, C.M. and Wernli, H. (2015) Importance of latent heat release in ascending air streams for atmospheric blocking. *Nature Geoscience*, 8, 610–614.

Pomroy, H.R. and Thorpe, A.J. (2000) The evolution and dynamical role of reduced upper-tropospheric potential vorticity in intensive observing period one of FASTEX. *Monthly Weather Review*, 128, 1817–1834.

Reed, R.J., Stoelinga, M.T. and Kuo, Y.-H. (1992) A model-aided study of the origin and evolution of the anomalously high potential vorticity in the inner region of a rapidly deepening marine cyclone. *Monthly Weather Review*, 120, 893–913.

Reinhardt, T. and Seifert, A. (2006) A three-category ice scheme for lmk. *COSMO Newsletter*, 6, 115–120 https://www.cosmo-model.org/content/model/documentation/newsLetters/newsLetter06/cnl6_reinhardt.pdf.

Rossa, A.M., Wernli, H. and Davies, H.C. (2000) Growth and decay of an extra-tropical cyclone's PV-tower. *Meteorology and Atmospheric Physics*, 73, 139–156.

Saffin, L., Methven, J., Bland, J., Harvey, B. and Sanchez, C. (2021) Circulation conservation in the outflow of warm conveyor belts and consequences for rossby wave evolution. *Quarterly Journal of the Royal Meteorological Society*, 147, 3587–3610.

Schäfler, A., Craig, G., Wernli, H., Arbogast, P., Doyle, J., McTaggart-Cowan, R. and Bramberger, M. (2018) Modification of potential vorticity near the tropopause by nonconservative processes in the the North Atlantic waveguide and downstream impact experiment. *Bulletin of the American Meteorological Society*, 99, 1607–1637.

Schemm, S. and Sprenger, M. (2015) Frontal-wave cyclogenesis in the North Atlantic–a climatological characterisation. *Quarterly Journal of the Royal Meteorological Society*, 141, 2989–3005.

Schemm, S. and Wernli, H. (2014) The linkage between the warm and the cold conveyor belts in an idealized extratropical cyclone. *Journal of the Atmospheric Sciences*, 71, 1443–1459.

Schemm, S., Wernli, H. and Papritz, L. (2013) Warm conveyor belts in idealized moist baroclinic wave simulations. *Journal of the Atmospheric Sciences*, 70, 627–652.

Shapiro, M. and Keyser, D. (1990) Fronts, jet streams, and the tropopause. In: *Extratropical Cyclones: The Erik Palmén Memorial Volume*. Boston, MA: American Meteorological Society, pp. 167–191.

Shaw, T., Baldwin, M., Barnes, E.A., Caballero, R., Garfinkel, C., Hwang, Y.-T., Li, C., O'gorman, P., Rivière, G. and Simpson, I. (2016) Storm track processes and the opposing influences of climate change. *Nature Geoscience*, 9, 656–664.

Simmons, A.J. (2022) Trends in the tropospheric general circulation from 1979 to 2022. *Weather and Climate Dynamics*, 3, 777–809.

Spreitzer, E., Attinger, R., Boettcher, M., Forbes, R., Wernli, H. and Joos, H. (2019a) Modification of potential vorticity near the tropopause by nonconservative processes in the ECMWF model. *Journal of the Atmospheric Sciences*, 76, 1709–1726.

Spreitzer, E., Attinger, R., Boettcher, M., Forbes, R., Wernli, H. and Joos, H. (2019b) Modification of potential vorticity near the tropopause by nonconservative processes in the ecmwf model. *Journal of the Atmospheric Sciences*, 76, 1709–1726 https://journals.ametsoc.org/view/journals/atsc/76/6/jas-d-18%-0295.1.xml.

Staff Members of the Univ. of Chicago. (1947) On the general circulation of the atmosphere in middle latitudes: a preliminary summary report on certain investigations conducted at the University of Chicago during the academic year 1946–1947. *Bulletin of the American Meteorological Society*, 28, 255–280.

Steinfeld, D., Boettcher, M., Forbes, R. and Pfahl, S. (2020) The sensitivity of atmospheric blocking to upstream latent heating – numerical experiments. *Weather and Climate Dynamics*, 1, 405–426.

Stendel, M., Francis, J., White, R., Williams, P.D. and Woollings, T. (2021) Chapter 15-The jet stream and climate change. In: Letcher, T.M. (Ed.) *Climate Change*, Third edition. Amsterdam, NL: Elsevier, pp. 327–357.

Steppeler, J., Doms, G., Schättler, U., Bitzer, H.W., Gassmann, A., Damrath, U. and Gregoric, G. (2003) Meso-gamma scale forecasts using the nonhydrostatic model LM. *Meteorology and Atmospheric Physics*, 82, 75–96.

Stoelinga, M.T. (1996) A potential vorticity-based study of the role of diabatic heating and friction in a numerically simulated baroclinic cyclone. *Monthly Weather Review*, 124, 849–874.

Teng, H. and Branstator, G. (2019) Amplification of waveguide teleconnections in the boreal summer. *Current Climate Change Reports*, 5, 421–432.

Thorncroft, C.D., Hoskins, B.J. and McIntyre, M.E. (1993) Two paradigms of baroclinic-wave life-cycle behaviour. *Quarterly Journal of the Royal Meteorological Society*, 119, 17–55.

Thorpe, A.J. and Bishop, C.H. (1995) Potential vorticity and the electrostatics analogy: Ertel—Rossby formulation. *Quarterly Journal of the Royal Meteorological Society*, 121, 1477–1495.

Thorpe, A.J. and Emanuel, K.A. (1985) Frontogenesis in the presence of small stability to slantwise convection. *Journal of Atmospheric Sciences*, 42, 1809–1824.

Vallis, G.K., Zurita-Gotor, P., Cairns, C. and Kidston, J. (2015) Response of the large-scale structure of the atmosphere to global warming. *Quarterly Journal of the Royal Meteorological Society*, 141, 1479–1501.

Wernli, H. and Davies, H.C. (1997) A lagrangian-based analysis of extratropical cyclones. I: the method and some applications. *Quarterly Journal of the Royal Meteorological Society*, 123, 467–489.

Wernli, H., Dirren, S., Liniger, M.A. and Zillig, M. (2002) Dynamical aspects of the life cycle of the winter storm 'Lothar' (24–26 December 1999). *Quarterly Journal of the Royal Meteorological Society*, 128, 405–429.

Whitaker, J.S., Uccellini, L.W. and Brill, K.F. (1988) A model-based diagnostic study of the rapid development phase of the President's day cyclone. *Monthly Weather Review*, 116, 2337–2365.

Winters, A.C. (2021) Kinematic processes contributing to the intensification of anomalously strong North Atlantic jets. *Quarterly Journal of the Royal Meteorological Society*, 147, 2506–2532.

Wirth, V. (2020) Waveguidability of idealized midlatitude jets and the limitations of ray tracing theory. *Weather and Climate Dynamics*, 1, 111–125.

Wirth, V. and Egger, J. (1999) Diagnosing extratropical synoptic-scale stratosphere-troposphere exchange: a case study. *Quarterly Journal of the Royal Meteorological Society*, 125, 635–655.

Wirth, V. and Polster, C. (2021) The problem of diagnosing jet waveguidability in the presence of large-amplitude eddies. *Journal of the Atmospheric Sciences*, 78, 3137–3151.

SUPPORTING INFORMATION

Additional supporting information can be found online in the Supporting Information section at the end of this article.